Accelerating glacier mass loss on Franz Josef Land, Russian Arctic

Whyjay Zheng[a,*], Matthew E. Pritchard[a], Michael J. Willis[b,c], Paul Tepes[d], Noel Gourmelen[d,e], Toby J. Benham[f], Julian A. Dowdeswell[f]

[a] *Department of Earth and Atmospheric Sciences, Cornell University, Ithaca, New York, USA*
[b] *Cooperative Institute for Research in Environmental Sciences, University of Colorado Boulder, Boulder, Colorado, USA*
[c] *Department of Geological Sciences, University of Colorado Boulder, Boulder, Colorado, USA*
[d] *School of Geosciences, University of Edinburgh, Edinburgh, UK*
[e] *Institut de Physique du Globe de Strasbourg (UMR 7516 CNRS), Universit de Strasbourg, Strasbourg, France*
[f] *Scott Polar Research Institute, University of Cambridge, Cambridge, UK*

Abstract

Franz Josef Land (FJL) in the Russian Arctic, is one of the fastest-warming regions in the Arctic but the glaciers there have not contributed significantly to sea level in the past. We analyze ice surface elevation data derived from satellite stereo imagery (WorldView and SPOT), radar altimetry (CryoSat-2), and a digitized 1953 cartographic map to calculate elevation change rates ($\frac{dh}{dt}$). Mass loss from FJL has doubled between 2011-2015 compared to 1953-2011/2015, increasing from a rate of -2.18 ± 0.72 Gt yr^{-1} to -4.43 ± 0.78 Gt yr^{-1}. This new rate between 2011-2015 also indicates the accelerated ice loss from the value during 2003-2009 from multiple studies using ICESat and GRACE. Despite the fact that glacier to glacier thinning rates are highly variable, we observe glacier thinning rates of up to 10 meters per year, and in general we find a trend of increased thinning from the NE towards the SW. Glacier retreat is widespread and has led to the creation of at least one new island. Historically, ice wastage from FJL is thought to have been relatively small, but accelerating ice loss may be the new normal for this archipelago in a warming Arctic.

*Corresponding author
Email address: wz278@cornell.edu (Whyjay Zheng)

Keywords: Franz Josef Land, Russian Arctic, cryosphere, climate change, DEM, dh/dt, glacier, ice cap, elevation change, ice loss, ArcticDEM, WorldView, SPOT-5, CryoSat-2

1. Introduction

Arctic air temperatures have increased at double the average global rate over the past few decades (e.g., Serreze & Francis, 2006; Pithan & Mauritsen, 2014). This has led to a corresponding loss of Arctic sea ice and warming of the ocean (Screen & Simmonds, 2010). Land ice in the Arctic is thought to be vulnerable to atmospheric warming and marine-terminating glaciers are affected by changes in ocean temperatures. Arctic air temperatures have increased unevenly (e.g., Walsh, 2009; Cohen et al., 2014) with warming in the Russian Arctic outpacing rates everywhere else except northern Alaska, particularly in winter (DJF) (Walsh, 2009). Although the Russian Arctic accounts for about 14% (51,800 km^2) of Arctic land ice (e.g., Radić et al., 2014), this region only contributed 8% of the entire Arctic land ice mass loss (-11 ± 4 Gt yr^{-1}) between 2003-2009 (Moholdt et al., 2012; Gardner et al., 2013). Numerical model simulations suggest that the glaciers and ice caps of the Russian Arctic islands may contribute 20-30 mm to global sea level rise by 2100 (Radić et al., 2014). Glaciers in the western hemisphere portion of the Arctic, including Greenland, the Canadian Arctic and Alaska, had higher ice loss rates than the Russian Arctic between 2003-2010 (e.g., Jacob et al., 2012; Gardner et al., 2013).

Ice mass changes across the Russian Arctic are spatially variable. Novaya Zemlya has the largest glacierized area (42.9% of the Russian Arctic ice) with an ice mass change rate of -340 ± 50 kg m^{-2} yr^{-1} between 2004-2009 (Moholdt et al., 2012), -320 ± 50 kg m^{-2} yr^{-1} between 2011 and 2014 (Sun et al., 2017), and -300 ± 60 kg m^{-2} yr^{-1} between 2012 and 2014 (Melkonian et al., 2016); Severnaya Zemlya in the east (32.4% of the Russian Arctic ice) has a lower rate of -78 ± 48 kg m^{-2} yr^{-1} between 2003 and 2009 (Moholdt et al., 2012). Franz Josef Land (abbreviated as FJL), the northernmost archipelago in the

Russian Arctic (Figure 1), consists of around 200 islands between $79 - 82°$N, and has a total surface area of 16,135 km^2 (Barr, 1995), roughly the same as the U.S. state of Hawaii. It is generally classified as a polar desert with an average annual precipitation of 228 mm w.e. (Moholdt et al., 2012; Sharov, 2010), a mean annual air temperature of $-12.4°$C, and summer air temperatures that hover around 0°C (Barr, 1995). Regional climate variation at each island is unknown due to a lack of weather stations. Land ice covered over 85% of the archipelago in 1957-59, equivalent to 13,735 km^2 (Grosswald et al., 1973); however, ice cover was recorded as 12,700 km^2 (24.7% of the Russian Arctic ice) in 2000-2010 by Moholdt et al. (2012). In contrast to the shrinkage of ice cover, past measurements suggest that FJL has been close to neutral in ice mass budget over the past decades. The mass budget derived from GRACE data was 0 ± 2 Gt yr^{-1} (0 ± 160 kg m^{-2} yr^{-1}) between 2003-2010 (Jacob et al., 2012) and -0.8 ± 1.3 Gt yr^{-1} (-63 ± 102 kg m^{-2} yr^{-1}) between 2004-2012 (Matsuo & Heki, 2013). The ICESat analysis by Moholdt et al. (2012) gives a slightly more negative value of -0.9 ± 0.7 Gt yr^{-1} (-71 ± 55 kg m^{-2} yr^{-1}) between 2004-2009, but the rate of loss is much lower than its nearest neighbors, Novaya Zemlya and Svalbard; the latter has an ice mass change rate of -130 ± 60 kg m^{-2} yr^{-1} between 2003-2009 (Gardner et al., 2013).

To better understand mass loss from the glaciers and ice caps of FJL and the change of mass loss rate since 2010, we produce a high-resolution map of ice elevation changes across the archipelago. We highlight similar variability to Sharov (2008) who found that elevation changes at adjacent glaciers could be very different. We produce our digital elevation models (DEMs) from along-track stereo optical satellite imagery collected as a time series, and resolve the details of FJL mass loss on a glacier-by-glacier basis across the entire region over 60 years. Our WorldView-derived DEMs are 2-m posting and have reduced errors on steep and rugged terrains compared to lower resolution techniques. This new method features comprehensive measurements on ice elevation, thus is more capable of detecting changes in a small region, e.g. ice loss rate variations between two adjacent glaciers. We additionally stack DEMs derived from

SPOT-5, CryoSat-2, and cartographic data with our DEMs in order to examine and extend the time series of elevation changes.

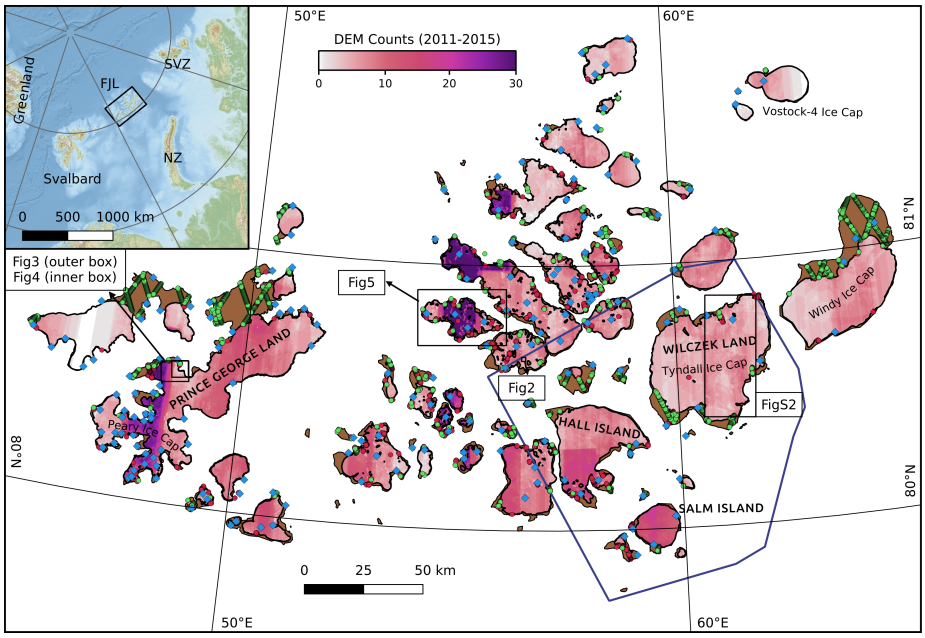

Figure 1: The coverage map of WorldView-derived DEMs over glacierized areas of Franz Josef Land (FJL), with names of islands (bold) and ice caps mentioned in this paper. Off-ice area is highlighted in brown. 18,447 ICESat points (red + green) are used for coregistering WorldView DEMs, and only 10,398 points (green) are used for the cartographic DEM. 185 ground control points (blue diamonds) are also used in georeferencing the cartographic DEM. The data coverage of 2007 SPOT-5 DEM is outlined by the blue polygon. The outline of 1953 cartographic DEM is not shown since it covers the whole area of FJL. The inset map shows the location of FJL and other islands in the Eurasian Arctic (NZ: Novaya Zemlya; SVZ: Severnaya Zemlya). The figure also serves as a reference map of the location of Figure 2, 3, 4, and 5.

2. Data

2.1. Elevations from WorldView Satellite Series

DEMs from multiple sources are compared in this study. The ArcticDEM (`https://www.pgc.umn.edu/data/arcticdem/`) is used as our primary data source. This is an initiative to provide open access 2-m DEMs across the entire Arctic (e.g., Noh & Howat, 2015). The DEMs were created from DigitalGlobe's WorldView-1, WorldView-2, and WorldView-3 optical stereo imagery using the software Surface Extraction with TIN-based Search-space Minimization (SETSM), and the details are described in Noh & Howat (2015). In the second release in late 2016, 564 strips were available for FJL. In this study, we use only 385 strips for which an "ICESat transformation vector" is provided within the metadata. We use the transformation vector to correct the DEMs with the best fit ICESat measurements (see section 3.1). All the DEMs were acquired between 2011 and 2015, with coverage shown in Figure 1.

In addition to ArcticDEM, we use other DEMs derived from WorldView imagery but not included in ArcticDEM. These additional DEMs are generated by NASA's Ames Stereo Pipeline (ASP) tool suite, which is suitable for many datasets including WorldView (e.g. (Moratto et al., 2010; Shean et al., 2016)). We generate 65 DEMs with a 3-m resolution for the period 2011-15 to provide more complete coverage in the study area.

2.2. Elevations from Cartographic Data, SPOT-5, and CryoSat-2

To compare WorldView DEMs with older elevation data, we use elevations from a digitized cartographic map and a SPOT-5 DEM. The Russian cartographic map was sourced from aerial photographs acquired in 1953. It was prepared and released online by de Ferranti (2014) with a spatial resolution of 90 m. The SPOT-5 archive GES_08-016 contains DEMs for the southeastern part of FJL, derived from stereo imagery (available at `https://theia-landsat.cnes.fr`). We use the dataset VILCSEK_LAND_ICE_CAP_V2 DEM from the archive. The DEM elevations are derived from imagery acquired on September 18, 2007, and are posted with a spatial resolution of 40 m.

We also analyze elevation changes from the CryoSat-2 L1b SARIn mode data in order to provided an independent assessment of the elevation change in addition to WorldView DEMs. The elevations were measured between June 1, 2011 and October 1, 2015, which is similar to the total time span of WorldView DEMs.

2.3. Coastlines and Glacier Outlines

We use the GSHHG 2.3.6 database (`http://www.soest.hawaii.edu/wessel/gshhg/`) for reference coastlines (Wessel & Smith, 1996). The contour of zero elevation from the cartographic DEM is used as the 1953 coastline. Glacier outlines in the 2000s are from the Randolph Glacier Inventory (RGI) version 3.0 (Pfeffer et al., 2014). Note that the glacier outlines for FJL have not changed in later versions, that is, they are identical to the latest RGI version 6.0 (released in July 28, 2017). Therefore, we create more recent and precise coastlines and glacier outlines between 2011-2015 using Landsat 8 images and ArcticDEM elevations and slopes. The new coastlines and glacier outlines help to recognize whether a negative ice elevation change is due to ice-surface thinning or the retreat of a marine-terminating glacier margin, and will be provided in the future to RGI or other established databases (e.g., Rastner et al., 2017).

2.4. Temporal Sea-Ice Concentration and Sea Surface Temperature

We use the COBE-SST2 data products (`http://www.esrl.noaa.gov/psd/`) for temporal sea-ice concentration (SIC) and sea surface temperature (SST) (Hirahara et al., 2014). The products are both released as a 1-degree grid with monthly means from January 1850 to December 2015. We calculate the time series of SIC and SST at FJL by averaging all pixels from 45°E to 65°E and from 80°N to 81°N (that is, 42 pixels). We average periods from JJA as summer records and from DJF as winter records. These datasets help provide insight into possible causes of any observed changes in FJL.

3. Methods

3.1. Coregistering and Filtering WorldView DEMs

We coregister all WorldView DEMs with ICESat returns over bedrock. 385 WorldView DEMs are from ArcticDEM dataset, each with an unique ICESat transformation vector. We simply add the transformation vector to the extent (x and y component) and the elevations (z component) of each DEM strip. For 65 ASP-derived WorldView DEMs, we used a modified approach from Willis et al. (2012) and Melkonian et al. (2016), which is described below.

The ICESat data are from release 531 of the Level-1B (GLA06) product (Zwally et al., 2014). The plane-filtered elevation product was processed and provided by Geir Moholdt, see Moholdt et al. (2012) and Moholdt et al. (2010b) for more details. The returns from off-ice areas are clipped using coastline data and ice outlines (both described in section 2.3), and are validated using Landsat and WorldView optical imagery. A total of 18,447 ICESat points are available for coregistering the DEMs (Figure 1), which is done using the Iterative Closest Point (ICP) routine (Beyer et al., 2014) that is implemented by the ASP (e.g., Melkonian, 2014). We use the "pc_align" tool in the ASP to generate an ICESat-coregistered point cloud from each DEM, and then use the "point2dem" tool in the ASP to translate the point cloud into GeoTIFF format. Each coregistered DEM in GeoTIFF format is checked with other coregistered DEMs covering the same area, for an erroneous ramp effect that can result from insufficient ICESat coverage. For DEMs with ramps we redo coregistration using other coregistered WorldView DEMs that cover the same off-ice areas as the target DEM. Table S1 lists all WorldView DEMs, the DEM dates, and the method used for coregistration.

To remove spurious elevations and improve the quality of the data, we apply a median filter using a window radius of 4 pixels to all the coregistered DEMs before any further analysis.

3.2. Assessing DEM Vertical Uncertainties

We individually assess each DEM for vertical uncertainty. Our approach, adapted from Carabajal & Harding (2005) and Willis et al. (2015), is to find the difference between the DEM and the ICESat elevations, and calculate the standard deviation after clipping outliers ($>$ 3 median absolute deviation away from the mean value, Figure S6). The standard deviation between ICESat and DEM elevations over the ice-free area is assigned as the DEM uncertainty. Since this value represents an error propagated from the linear combination of ICESat and DEM measurements, we adopt it as a conservative estimate because it should be larger than only the DEM intrinsic uncertainty itself.

The median uncertainty of ArcticDEM and other WorldView-derived DEMs are $\pm$0.89 m and $\pm$0.74 m respectively. We arbitrarily select DEMs with an absolute value of uncertainty $<$ 3 m and a mean offset from ICESat data $<$ 2 m. This yields a collection of 432 WorldView DEMs, which have uncertainty between $\pm$0.17 and $\pm$2.9 m (listed in Table S1).

As a comparison, the vertical precision of ICESat data is better than 0.05 m under optimal conditions (Fricker et al., 2005), $\sim$0.15 m in gently sloping topography (Zwally et al., 2002; Shuman et al., 2006), and within 1 m on steeper terrains in the Russian Arctic (Moholdt et al., 2010b, 2012). Uplift rates due to glacial isostatic adjustment are expected to be an average of 1.1 mm yr^{-1} in Franz Josef Land (Forman et al., 2004), and thus are within the DEM uncertainties. We use DEMs from all seasons, and so seasonal snowfall is included in both the ice surface and bedrock elevations. The effect of seasonal snow is expected to be less than 1 m (Willis et al., 2015) in this polar desert but it could be larger in areas with steeper slopes that have higher errors (e.g., Moholdt et al., 2012).

3.3. Elevation Change Rate during WorldView Time Span (2011-2015)

All the WorldView DEMs are warped into a common 15-m grid in polar stereographic coordinate system (EPSG:3413) using bilinear interpolation before any comparison. Since WorldView DEMs are densely distributed over FJL

between 2011 and 2015 (Figure 1), we sort these DEMs by time, stack the elevations, and apply weighted linear regression on the time series of elevations (e.g. Melkonian et al., 2013; Wang & Kääb, 2015; Durkin et al., 2017). The $\frac{dh}{dt}$ (i.e. the slope of linear regression) and its uncertainty (i.e. the error estimate of the slope) is calculated on a cell-by-cell basis.

The $\frac{dh}{dt}$ from weighted linear regression of the WorldView DEMs is further processed for noise removal and data improvement, including smoothing and void-filling. The $\frac{dh}{dt}$ map is firstly smoothed by the same median filter from filtering WorldView DEMs. Then we fill all the no-data holes which occupy less than 300 pixels using bilinear interpolation. Figure 2a and c show the comparison before and after these processes. For the corresponding uncertainty map, we don't smooth these values but still fill voids. To get the most conservative estimate, the uncertainty of all the pixels in a hole is determined by the maximum uncertainty of all the surrounding pixels, as shown in Figure 2b and d.

The local off-ice (i.e., bedrock) $\frac{dh}{dt}$ is used for bias checking in the $\frac{dh}{dt}$ map. At Eva-Liv Island, the average local off-ice WorldView $\frac{dh}{dt}$ is 0.94 m yr^{-1} with an uncertainty of 0.11 m yr^{-1} (Figure S8); an estimate that deviates from zero elevation change. Thus, We subtract 0.94 m yr^{-1} from the WorldView $\frac{dh}{dt}$ and add 0.11 m yr^{-1} to the uncertainty of WorldView $\frac{dh}{dt}$ at Eva-Liv region for correcting the off-ice bias.

Note that if there are equal or less than three elevation records available at a single pixel, we don't apply weighted linear regression because any unreliable elevation would contribute a large error on the fitting slope, i.e. $\frac{dh}{dt}$. Instead, we simply calculate $\frac{dh}{dt}$ by subtracting the earliest reliable elevation from the latest reliable elevation, and then dividing by the time between these two records. Please see section 3.4 for how we verify the elevations and prepare mosaicked DEMs in the full extent of FJL from WorldView DEMs.

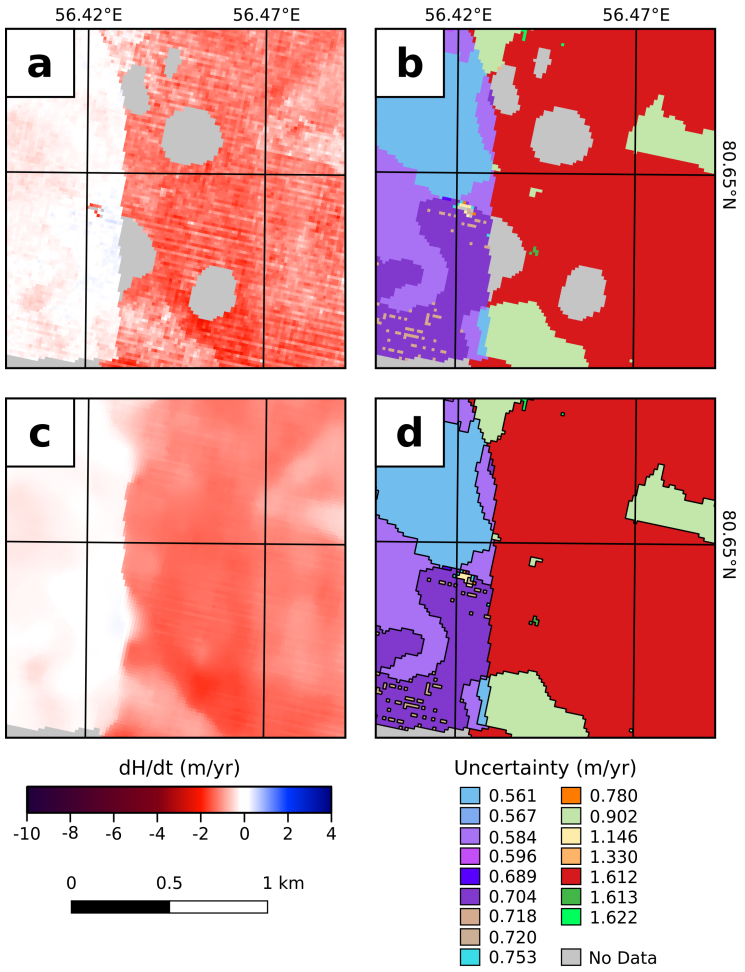

Figure 2: Steps in post-processing the 2011-15 WorldView $\frac{dh}{dt}$ map that is from weighted linear regression. (a) The regional details of the raw $\frac{dh}{dt}$ map in Figure S8 (location shown in Figure 1). Pixels with no-data values are shown in gray. (b) The uncertainties of the raw $\frac{dh}{dt}$ map. Color codes represent values from different DEM sets used in the weighted linear regression. (c) Smoothed and void-filled $\frac{dh}{dt}$ map which is identical to Figure 7, and (d) the corresponding void-filled uncertainty map. The voids are filled using bilinear interpolation for the $\frac{dh}{dt}$ map and using the maximum uncertainty of the adjacent pixels for the uncertainty map. See section 3.8 for further details on how the bulk uncertainty is calculated. The grid spacing for all the products is 15 m.

3.4. Collecting the Earliest and the Latest Reliable Elevations from WorldView DEMs

We collect measurements from WorldView DEMs that reflect the earliest reliable elevations during the WorldView time span (2011-2015), in order to compare with the 1953 cartographic data and the 2007 SPOT-5 DEM on a cell-by-cell basis. To begin with, we sort all DEMs by date, then create a blank DEM with a resolution of 15 m and an extent that covers the entire study region. Starting from the earliest scene, we read each WorldView-derived DEM and warp it into the same grid spacing and extent of the blank DEM. The linear interpolation is used for resampling because it best approaches the flat ice surface. The pixel values of the resampled DEM are thus used to fill in the blank DEM except for no-data pixels. Once a pixel in the blank DEM is filled, it does not change its value unless it fails on the check of quality control, which is described in the next paragraph. That is, as we read more DEMs, the blank DEM will be gradually filled, and every pixel represents the earliest available WorldView elevation.

To ensure that the WorldView elevation entered in the blank DEM is correct, we adopt an approach called "Elevation Verification from Multiple DEMs", abbreviated as EVMD to be applied when a pixel in the blank DEM is filled. A pixel can only pass the EVMD if there are 2 or more source DEMs that agree with each other, with a maximum arbitrary difference of 10 m. The arbitrary threshold is selected since this is roughly the maximum ice thinning change rate we observed using weighted linear regression from all WorldView DEMs. When a pixel in the blank DEM is filled with the earliest elevation and we find the second DEM that covers the same pixel, we read the pixel value from the second DEM and compare it with the earliest elevation. If the difference is less than 10 m, then the pixel passes the EVMD and we keep the earliest elevation record. Otherwise, it fails the verification, with the first elevation temporarily being kept. When the pixel value from the third DEM is loaded, we compare it with previous values (the first and the second measurements). Whichever has the difference less than 10 m from the third measurement will pass the EVMD and

replaces the pixel value in the blank DEM. If it fails again, one more elevation from another DEM is needed for further verification, and we repeat the process until it passes the EVMD or there are no more DEMs available. Once a pixel passes the EVMD, it is considered complete, and the value won't be changed. Finally, the associated date and uncertainty at this pixel from the source DEM are separately recorded in a raster file with an identical extent and grid spacing. Figure 3a and 3b show how EVMD can effectively remove most DEM artifacts in a mosaicked product.

We use this approach to make two separate DEMs for the earliest and the latest WorldView elevations. To make the latest WorldView elevation product, we simply reverse the sorting order. 97.9% of the pixels in both final DEM products are filled with elevations after going through all 432 WorldView DEMs, and 94.4% of all the pixels pass the EVMD. In Figure 3e, colored codes are used to indicate whether the pixel passes the EVMD or not.

The mosaicked DEMs are further processed in order to remove the spurious $\frac{dh}{dt}$ results due to the noise in the elevation data (e.g. clouds and shadowed area) and the lack of multiple DEMs. We manually mask out spurious elevations (i.e. changing sharply from neighboring pixels) that occupy more than 4-by-4 pixels (some examples outlined as green in Figure 4). The output rasters are then processed by a median filter using a window radius of 4 pixels for small-sized noise removal (Figure 4b). The final DEM products are thus used for comparing with other datasets and completing the WorldView $\frac{dh}{dt}$ map where there are insufficient measurements for weighted linear regression at an individual pixel. The complete steps of processing the WorldView DEMs are also shown in Figure S3.

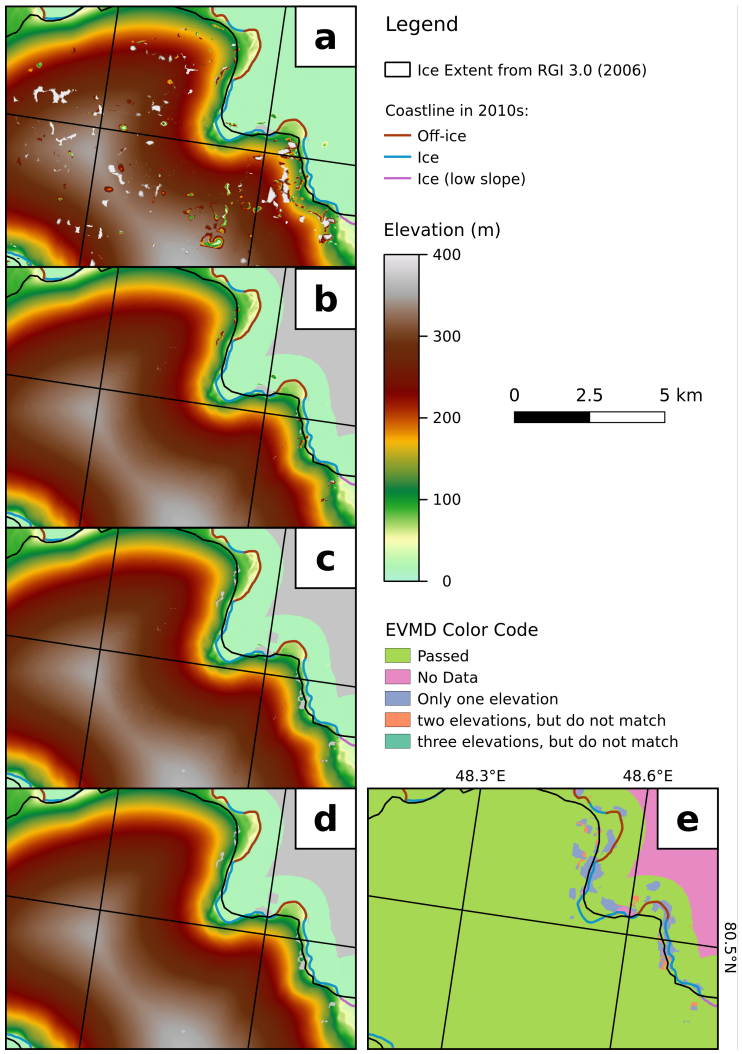

Figure 3: Quality improvement when mosaicking WorldView-derived DEMs. (a) Mosaicking without the EVMD (Elevation Verification from Multiple DEMs). (b) Mosaicking with the EVMD. (c) After manually removing large-sized elevation outliers. (d) After applying the median filter. (e) The color codes represent different exit status of the EVMD. Processing details are available in section 3.4 and Figure S3. Black lines indicate the ice outline from RGI (in 2006). Brown and blue lines are the off-ice and ice coastline in 2011-15 respectively, mapped using WorldView DEMs and Landsat imagery. The location of this figure is shown in Figure 1.

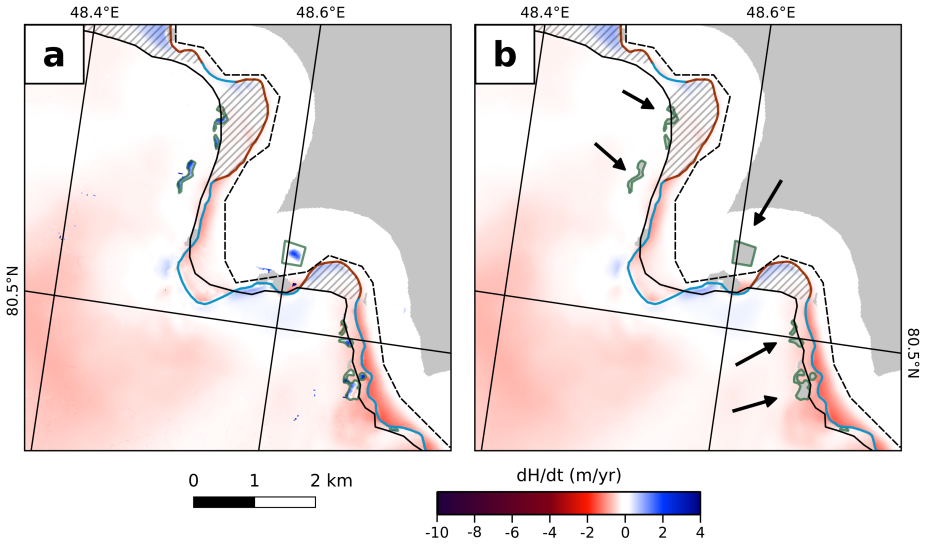

Figure 4: Noise reduction of the $\frac{dh}{dt}$ map between 1953 (cartographic) and 2011/15 (WorldView). (a) Before outlier removal and median filter. (b) After outlier removal and median filter. The areas indicated by arrows are recognized as outliers and manually removed. Black lines indicate the ice outline from RGI (in 2006) and the hatched areas are off-ice regions. Brown and blue lines are the off-ice and ice coastline in 2012/13 respectively, mapped using WorldView DEMs and Landsat imagery. Black dashed line indicates the coastline in 1953, mapped using the cartographic DEM. The location of this figure is shown in Figure 1.

3.5. Coregistering the 1953 Cartographic DEM

We coregister the 1953 cartographic DEM to the ICESat reference frame to compare with recent WorldView DEMs and the 2007 SPOT-5 DEM using the procedure of Willis et al. (2015). First, the DEM is converted from the EGM96 geoid to the WGS84 ellipsoid, as this is within 50 cm of the ICESat ellipsoid. The converted cartographic DEM has some discrepancies with the ICESat elevations. For example, 1,142 out of all 18,447 ICESat elevations differ by over 40 m from the cartographic DEM. This can result in "contamination" of the DEM transformation vector as we try to align the cartographic DEM including these outliers to the ICESat elevations. We therefore need to refine the 18,447 ICESat points and select those that can be paired with reliable elevations in the cartographic DEM.

The cartographic DEM is firstly coregistered to all all 18,447 ICESat elevations using ASP, which is described in section 3.1. Then the difference between the coregistered DEM and ICESat elevations are calculated in QGIS. We remove ICESat elevations that differ from the DEM values by more than 2 standard deviations, and use the remaining points to coregister the original cartographic DEM again. The standard deviation of the difference between the re-coregistered DEM and the culled set of ICESat elevations thus decreases because the control points that do not match cartographic elevation are removed. We iterate the process of refining ICESat elevation and re-coregistration until the standard deviation does not significantly decrease.

The standard deviation is 23.5 m in the first round, and decreases into 4-5 m after the 12^{th} round. We arbitrarily stop at the 20^{th} round with a standard deviation of 4.3 m, using a total 10,398 ICESat points (Figure 1). The DEM uncertainty is thus re-calculated using all 18,447 ICESat elevations, which yields an uncertainty of 10.5 m. Due to its large horizontal uncertainties (e.g. Figure 5), the coregistered 1953 DEM is further georeferenced by 185 additional ground control points, which are set at rock features such as cliff tops or nunataks observed in both the cartographic DEM and WorldView DEMs (Figure 1). The uncertainty of the georeferenced cartographic DEM decreases into 9.2 m. The

complete steps of processing the Cartographic DEM are in Figure S4.

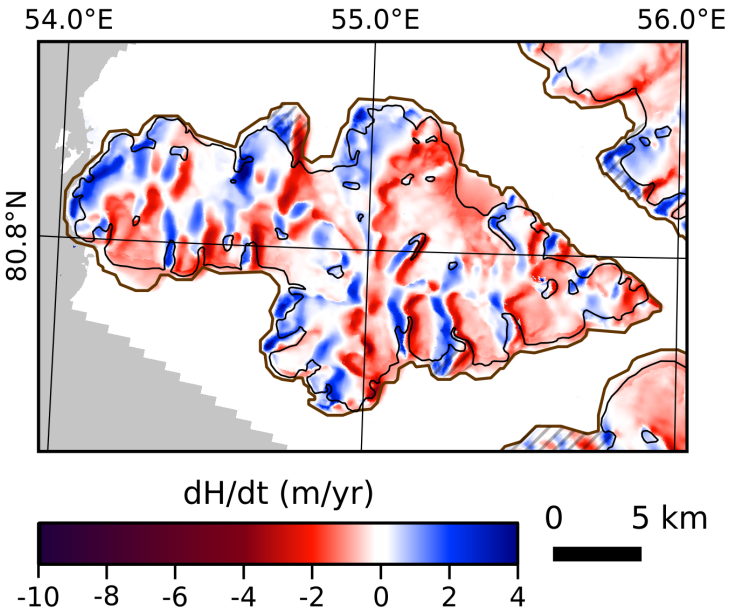

Figure 5: $\frac{dh}{dt}$ map of a small region of FJL (location shown in Figure 1) between the coregistered but pre-georeferenced 1953 cartographic DEM and the earliest WorldView elevations from 2011/15. The interleaved positive and negative $\frac{dh}{dt}$ changes are due to the horizontal errors of the cartographic DEM. The $\frac{dh}{dt}$ map of the same region but between the properly georeferenced cartographic DEM and the earliest WorldView elevations can be found in Figure 7. Brown and black outlines indicate the 1953 coastlines and RGI glacier outlines respectively, and hatched areas indicate major off-ice regions.

3.6. Masking and Coregistering the 2007 SPOT-5 DEM

The first task of processing the 2007 SPOT-5 DEM is to mask out clouds and other spurious elevations for a better coregistration. We mask the DEM using the following several steps, using the SAGA tools within QGIS:

1. Apply a Laplace of Gaussian (LoG) filter to the DEM to generate the mask file, and flip all negative values in the mask file to positive. The LoG filter (named as "Laplacian filter" in the SAGA toolkit) is a standard algorithm for edge detection (Jähne, 2005, Ch. 12). The standard kernel of the Laplace operator is used:

$$L = \begin{bmatrix} 0 & -1 & 0 \\ -1 & 4 & -1 \\ 0 & -1 & 0 \end{bmatrix} \tag{1}$$

   A pixel classified as an edge (that is, with its value changing sharply from adjacent pixel values) is regarded as a bad pixel to be masked. After applying the LoG filter and flipping all negative values, the edge thus contains high pixel values in the mask file.

2. Apply a median filter using a window radius of 4 pixels to the mask file. Clouds make small-scale anomalies relative to the topography (Figure 6a). Therefore, a great concentration of edges is expected and clouds transform to a bright (high pixel value) region in the LoG-filtered image. We apply the median filter to remove high frequency noise and connect the densely distributed edges into a single region representing cloud coverage. The window radius at 4 pixels is used as we want to remove noise spanning only a few pixels.

3. Select pixels with LoG-filtered values > 8 and convert the mask file into a binary raster. The threshold value is determined by comparing the filtered image and the associated orthoimage since the rough extent of cloud coverage can be seen in the latter. All the pixels whose value is larger than the threshold value (which is 8 for the SPOT-5 DEM) are selected as cloud-covered regions.

4. Apply morphological filters on the binary mask file to fine tune the mask region (Jähne, 2005, Ch. 18). The optimal combination of filters and window size is hard to determine and often varies case by case (e.g., Ismail & Jaafar, 2013). Thus, we manually test different combinations and determine the best one by comparing the filtered mask region to noisy area in the raw DEM. In the best combination, four morphological filters are applied in the following sequence: dilation radius of 10 pixels; erosion radius of 13 pixels; dilation radius of 16 pixels; and erosion radius of 8 pixels. The first dilation and erosion combination closes small holes in the mask and removes small-sized erroneous selections. The second dilation and erosion pair expands the mask for being more conservative but keeps large holes in the mask since they are large enough to be considered as true elevations.
5. Apply the binary mask to the original DEM.

Next, we convert the masked DEM from geoid to ellipsoidal heights (WGS84), and then we coregister it using 2,561 ICESat elevations which are inside the extent of the SPOT-5 DEM. The filtered DEM after these steps is shown in Figure 6b, with the spurious regions masked. The corresponding $\frac{dh}{dt}$ map (using DEM differencing, see section 3.7 for details) between it and the earliest collection of WorldView elevations is shown in Figure 6c. As seen from the $\frac{dh}{dt}$ map, the DEM heights at some places are doubtful and result in unrealistic $\frac{dh}{dt}$ values (e.g. deep-blue areas in Figure 6c).

To further mask out the suspicious elevations (most likely due to clouds or featureless surfaces), we set up thresholds based on the elevations from the 1953 cartographic DEM and the earliest WorldView elevations. (Durkin et al., 2017). We assume that the year of earliest WorldView elevations is averaged to be 2013, and calculate the estimated elevation in 2007 assuming a steady $\frac{dh}{dt}$ between 1953 and 2013 on a cell-by-cell basis:

$$h_{2007} = h_{1953} + \frac{2007 - 1953}{2013 - 1953}(h_{2013} - h_{1953}) = h_{1953} + 0.9(h_{2013} - h_{1953}) \quad (2)$$

where h_{1953} is the cartographic DEM elevation, h_{2013} is the earliest WorldView elevation. Any elevation that deviates by more than $h_{2007}{}^{+8}_{-4}$ m is discarded. The masked DEM and the corresponding $\frac{dh}{dt}$ map are shown in Figure 6d and 6e respectively, which masks out the major blue outliers in Figure 6c. The vertical uncertainty of the final SPOT-5 DEM is ± 1.9 m, assessed using the same approach for WorldView DEMs (section 3.2). The complete steps of processing the SPOT-5 DEM are also outlined in Figure S5.

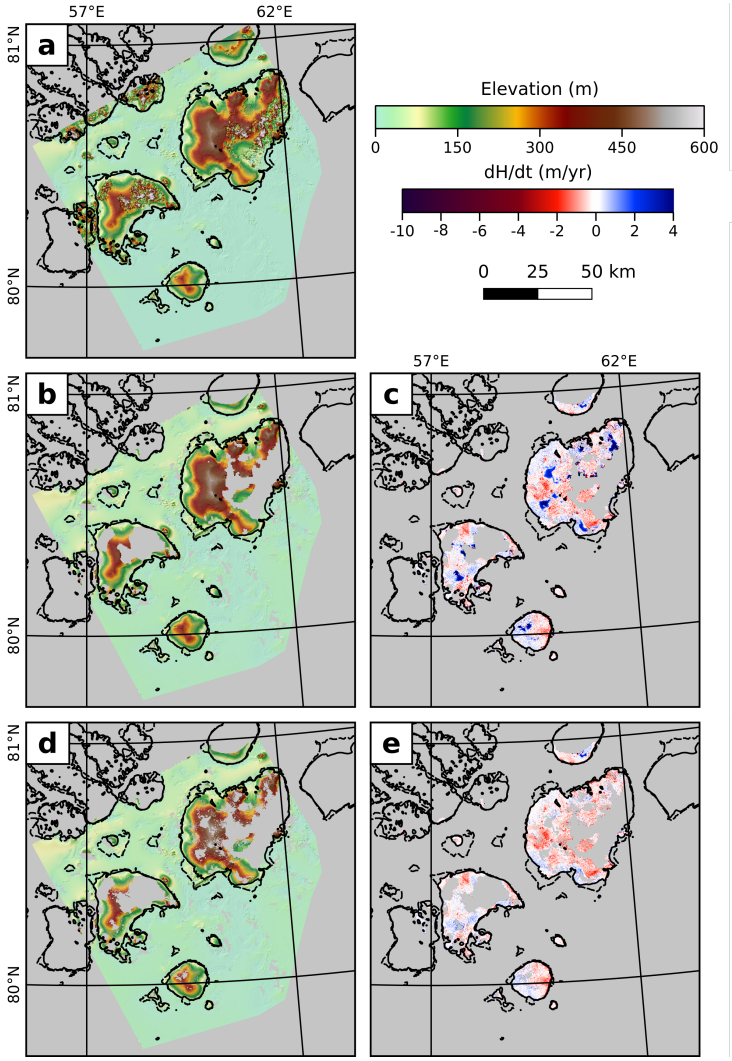

Figure 6: (a) Raw SPOT-5 DEM from September 18, 2007. The location of the DEM is shown in Figure 1. (b) The masked SPOT-5 DEM processed by a filter which is specifically designed for the removal of disrupted elevations due to cloud coverage. The DEM is coregistered with ICESat elevations. The details of the filter are available in section 3.6 and Figure S5. (c) $\frac{dh}{dt}$ map using DEM differencing, between the SPOT-5 DEM and the earliest collection of WorldView elevations. Artifacts with high $\frac{dh}{dt}$ values are scattered the ice caps. (d) The further masking of SPOT-5 DEM using time-dependent height thresholds. The details are also available in section 3.6. (e) The corresponding $\frac{dh}{dt}$ map between the final SPOT-5 DEM product and the earliest collection of WorldView elevations.

3.7. Elevation Change Rate between 1953 and 2011/15

To compare with the WorldView data, the 1953 cartographic DEM and the 2007 SPOT-5 DEM are warped into a 15-m grid, using bilinear interpolation. Because the limited temporal coverage does not permit weighted linear regression, we simply calculate $\frac{dh}{dt}$ using DEM differencing, which is to subtract a DEM elevation from another on a cell-by-cell basis, followed by division by the time span between the two elevation records. We apply DEM differencing between 1953 and 2007 (the cartographic DEM to the SPOT-5 DEM), between 1953 and 2011/15 (the cartographic DEM to the earliest collection of WorldView elevations), and between 2007 and 2011/15 (the SPOT-5 DEM to the earliest collection of WorldView elevations).

3.8. Ice Mass Budget

Once the $\frac{dh}{dt}$ maps are calculated, we integrate over the glacierized region to obtain the estimated annual ice volume and mass change. Each pixel in the $\frac{dh}{dt}$ map has the estimate of elevation change and the uncertainty calculated from DEM differencing or weighted linear regression. To find the bulk annual ice volume change ($\frac{dV}{dt}$), we simply sum up the product of $\frac{dh}{dt}$ and ground-projected pixel coverage (a, that is, the square of spatial resolution) through all pixels over a specific region:

$$\frac{dV}{dt} = \sum_i a\Big(\frac{dh}{dt}\Big)_i \tag{3}$$

a is 225 m for all our $\frac{dh}{dt}$ products since the grid spacing is 15 m. For the period between 1953 and 2011/15, the region is defined by the coastlines in 1953 because of the lack of ice boundary at that time. For the period in 2011-15, the ice boundary from RGI in 2001-2006 is used.

When calculating the error of $\frac{dV}{dt}$, we need to know how independent each $\frac{dh}{dt}$ measurement is (e.g., Melkonian, 2014). In this paper we assume that the measurements from the same DEM set are mutually dependent (i.e. they share a common error because they are calculated from the same DEM set), and the

measurements from different DEM sets can be treated independently. Figure 2d shows the void-filled uncertainty map and the color codes represent different uncertainty values, which also indicates the source DEM set. Once we group the uncertainties as outlined in black, the bulk uncertainty of $\frac{dV}{dt}$ is calculated by

$$\sigma_{\frac{dV}{dt}} = \sqrt{\sum_i \Big(\sum_j a \big(\sigma_{\frac{dh}{dt}}\big)_{ij} \Big)^2} \tag{4}$$

where i and j refer to the index of each error group and each pixel in the same error group respectively.

The annual ice mass change $\frac{dM}{dt}$ is thus converted from the $\frac{dV}{dt}$ using an ice density ρ of 850 kg m $^{-3}$ and an uncertainty σ_ρ of 60 kg m $^{-3}$ (Huss, 2013), an estimate for most cases since there is no local firn pack data. The uncertainty of $\frac{dM}{dt}$ is calculated assuming independent variables:

$$\sigma_{\frac{dM}{dt}} = \frac{dM}{dt} \sqrt{\Big(\frac{\sigma_{\frac{dV}{dt}}}{\frac{dV}{dt}}\Big)^2 + \Big(\frac{\sigma_\rho}{\rho}\Big)^2} \tag{5}$$

All the uncertainties reported in this paper, e.g. $\frac{dh}{dt}$, $\frac{dV}{dt}$, and annual ice mass change, are at 95% confidence level (2 standard errors).

3.9. Processing CryoSat-2 $\frac{dh}{dt}$

We apply swath processing to the interferometric mode of CryoSat-2 data to generate surface elevation (Gourmelen et al., 2017a), rates of elevation change at 500 m resolution and a mass balance estimate (Foresta et al., 2016). $\frac{dh}{dt}$ is calculated using a plane-fit approach on a 500m grid posting; for each pixel, we model elevation using a linear relationship in space and time:

$$z(x, y, t) = c_0 x + c_1 y + \frac{dh}{dt} t + c_2 \tag{6}$$

where x, y and t are easting, northing, and time, respectively. The time-dependent coefficient retrieved from the model fit is the linear rate of surface elevation change for each given pixel. Each observation is assigned a weight

according to the power returned for each pixel, as in Gourmelen et al. (2017b). We iteratively fit the model to the data using 3σ clipping until there are no more outliers. The formal uncertainty on each pixel's rate of elevation change is extracted from the model covariance matrix P:

$$P = \mathrm{cov}(p) = G^{-1}\mathrm{cov}(z)[G^{-1}]^T \tag{7}$$

where z are the input elevations, p is the vector of coefficients $[c_0\ c_1\ c_2]$ of the model parameters and $G = [x\ y\ t\ 1]$ is the model matrix. We simplify the data covariance matrix $\mathrm{cov}(z)$ to a variance matrix whose diagonal values are the squared elevation differences between the observed and modeled estimates $(z - z')^2$. The square root of the diagonal elements of P represents the standard deviations of the model parameters p.

To better compare CryoSat-2 $\frac{dh}{dt}$ with WorldView $\frac{dh}{dt}$, the CryoSat-2 $\frac{dh}{dt}$ map is masked by a series of criteria for noise removal:

1. The absolute value of $\frac{dh}{dt}$ is equal or larger than 20 m yr^{-1}.
2. The uncertainty of $\frac{dh}{dt}$ is equal or larger than 2 m yr^{-1}.
3. 8 adjacent pixels (N) are used in this step. The pixel is masked if any of the following statements is true:
   - There is no or only one valid (not No-Data) value in the adjacent pixels.
   - $|\frac{dh}{dt} - mean(N)| \leq T_1\sigma_N$
   - $max(N) - min(N) \leq T_2$

   where T_1 and T_2 are determined by grid search. This and the next step are modified from Fahnestock et al. (2016).
4. Mask out all pixels with only equal or less than 2 valid adjacent pixels.

We perform a grid search to find the optimal T_1 and T_2 given the trade-off between how well the remaining pixels match the WorldView $\frac{dh}{dt}$ and how many pixels are left.

4. Results

4.1. Elevation Changes and Ice Mass Loss Between 1953 and 2011/15

DEM differencing between the cartographic DEM and the earliest World-View elevations (i.e., 1953 to 2011/15) (Figure 7a and 8a) shows that about 62.7% of the ice surface area at FJL has thinned whereas 37.3% has thickened. We note that this calculation includes both ice-free and ice-covered land areas because of the lack of a precise land-terminating glacier boundary in 1953. The data covers 98.29% of the land area indicated by the 1953 coastline. The bulk ice volume change rate is calculated by assuming the average $\frac{dh}{dt}$ over the entire land area, yielding -2.57 ± 0.77 km^3 yr^{-1}. The ice mass change rate is then calculated from the volume loss and shows a negative value of -2.18 ± 0.72 Gt yr^{-1}. This value corresponds to a mean ice mass balance of -180 ± 59 mm w.e. yr^{-1} using the ice outline in 2001-2006 from RGI as the total glacierized area. Note that this is an overestimated value since the glacierized area has been shrinking since 1953. 15 marine-terminating glaciers with $\frac{dh}{dt}$ rates as high as -2 to -4 m yr^{-1} dominate the ice mass budget.

Most thickening occurs at ice caps that include no fast-flowing outlet glaciers indicated by topography and surface morphology. A prominent example is the Windy Ice Cap (Figure 7a, and Moholdt et al., 2012), the biggest and eastern-most ice cap in FJL, with a thickening rate around 1 m yr^{-1}.

Marine-terminating glacier fronts have commonly retreated 1-3 km across the archipelago, observed as a red "rind" of the ice outline in Figure 12. In the neighboring archipelagos of Svalbard, Novaya Zemlya and Severnaya Zemlya (e.g., Dowdeswell & Williams, 1997; Grant et al., 2009), the rapid advance and slow subsequent retreat of surging tidewater glacier termini provide a complication to climate-forced retreat. However, there is no clear evidence of past glacier surging in FJL (Dowdeswell & Williams, 1997; Dowdeswell et al., 2010).

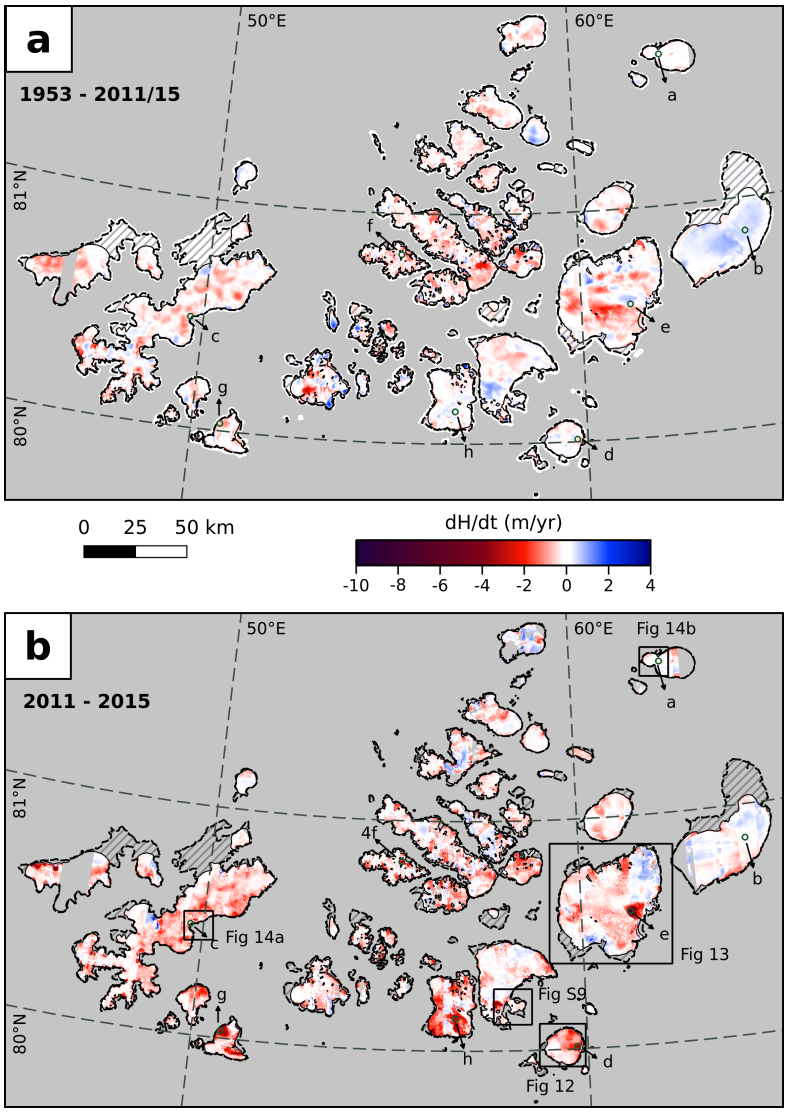

Figure 7: (a) $\frac{dh}{dt}$ at Franz Josef Land, between 1953 (cartographic DEM) and 2011/15 (earliest WorldView elevations). (b) $\frac{dh}{dt}$ map during 2011-2015, from WorldView DEMs. Dashed outlines indicate the coastline in 1953 and black outlines are ice boundaries from Randolph Glacier Inventory version 3.0 (Pfeffer et al., 2014) in 2001-2006. Ice-free land surface is shown by hatching region, and no-data pixels are shown in gray. The black boxes in (b) show the extent of Figures 12, 13, 14, and S9. The sample location of 8 time series shown in Figure 11 are also marked in this figure, labeled a to h.

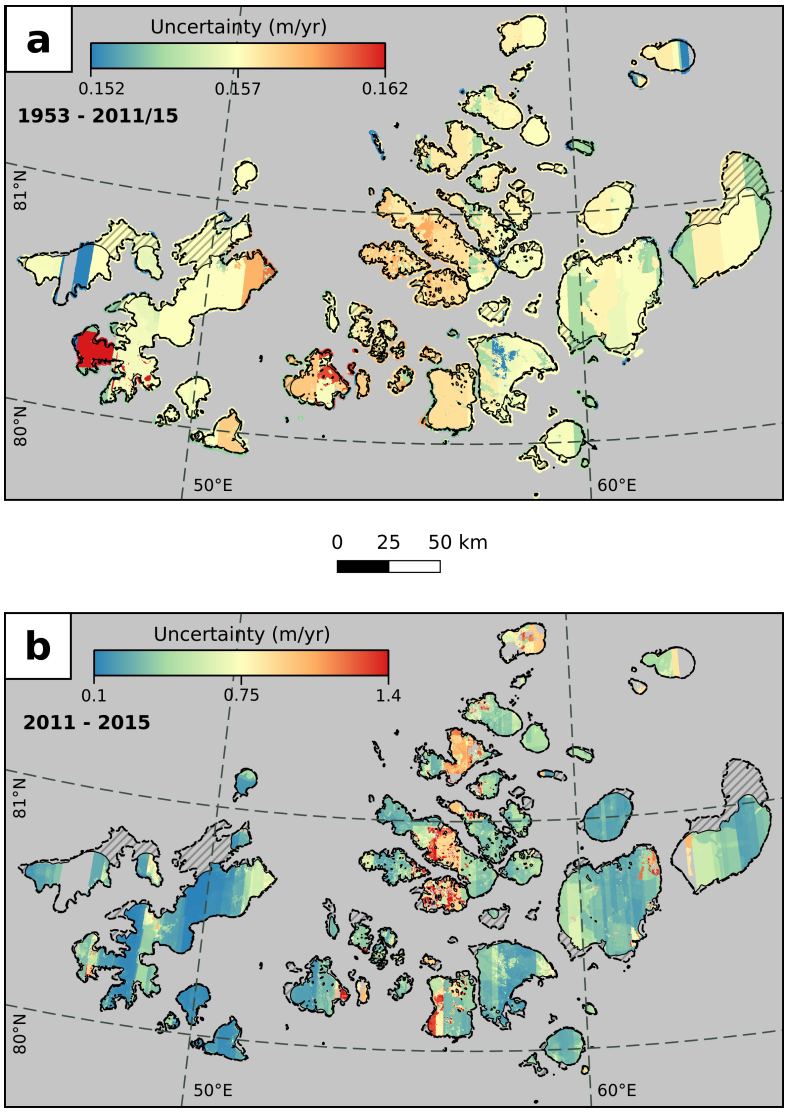

Figure 8: (a) The uncertainty (1-sigma) of $\frac{dh}{dt}$ between 1953 (cartographic DEM) and 2011/15 (earliest WorldView elevations), derived from the off-ice vertical error of both datasets, following the rules of error propagation. (b) The uncertainty (1-sigma) of $\frac{dh}{dt}$ during 2011-2015, using WorldView DEMs. Note the different scale used in each color ramp.

4.2. Elevation Changes and Ice Mass Loss Between 2011 and 2015

The WorldView $\frac{dh}{dt}$ (2011-2015) combines DEM differencing with the regression model and covers 91.9% of the RGI glacierized area of FJL. 75.1% of the ice caps and glaciers were thinning (Figure 7b and 8b) between 2011 and 2015; the area of thinning has expanded by about 12% compared to the area of thinning observed over the last 60 years. The average $\frac{dh}{dt}$ rate is -0.429 ± 0.044 m yr^{-1}, which, multiplied by the glacierized area, provides a loss rate of -5.21 ± 0.54 km^3 yr^{-1}. This corresponds to a mean ice mass balance of -364 ± 64 mm w.e. yr^{-1}, or an ice mass change rate of -4.43 ± 0.78 Gt yr^{-1}.

As an independent assessment of the WorldView $\frac{dh}{dt}$, we compare $\frac{dh}{dt}$ from CryoSat-2 altimeter elevations between 2011-2015. The CryoSat-2 $\frac{dh}{dt}$ map (Figure 9a) covers 76% of the RGI glacierized area, with an extensive coverage of the interior and of the rapidly thinning margins of the ice caps. It has a larger spatial resolution of 500 m but reveals similarity with WorldView $\frac{dh}{dt}$ in the locations of some fast-thinning glaciers and the large-scale spatial pattern of ice mass loss (see section 5.3). Given the dynamic nature of some of the observed change the relationship between surface elevation change and topography is complex. Hence we do not apply an elevation-based regionalization method (Foresta et al., 2016) but simply scale our measured volume change by the ratio between the total glacierized area and the area covered by our measurements. The ice budget derived from CryoSat-2 is -321 ± 57 mm w.e. yr^{-1} or -3.9 ± 0.7 Gt yr^{-1}. This is in agreement with the WorldView estimate within errors. Remaining differences between the two estimates may be related to the difference in spatial and temporal sampling between CryoSat-2 and WorldView.

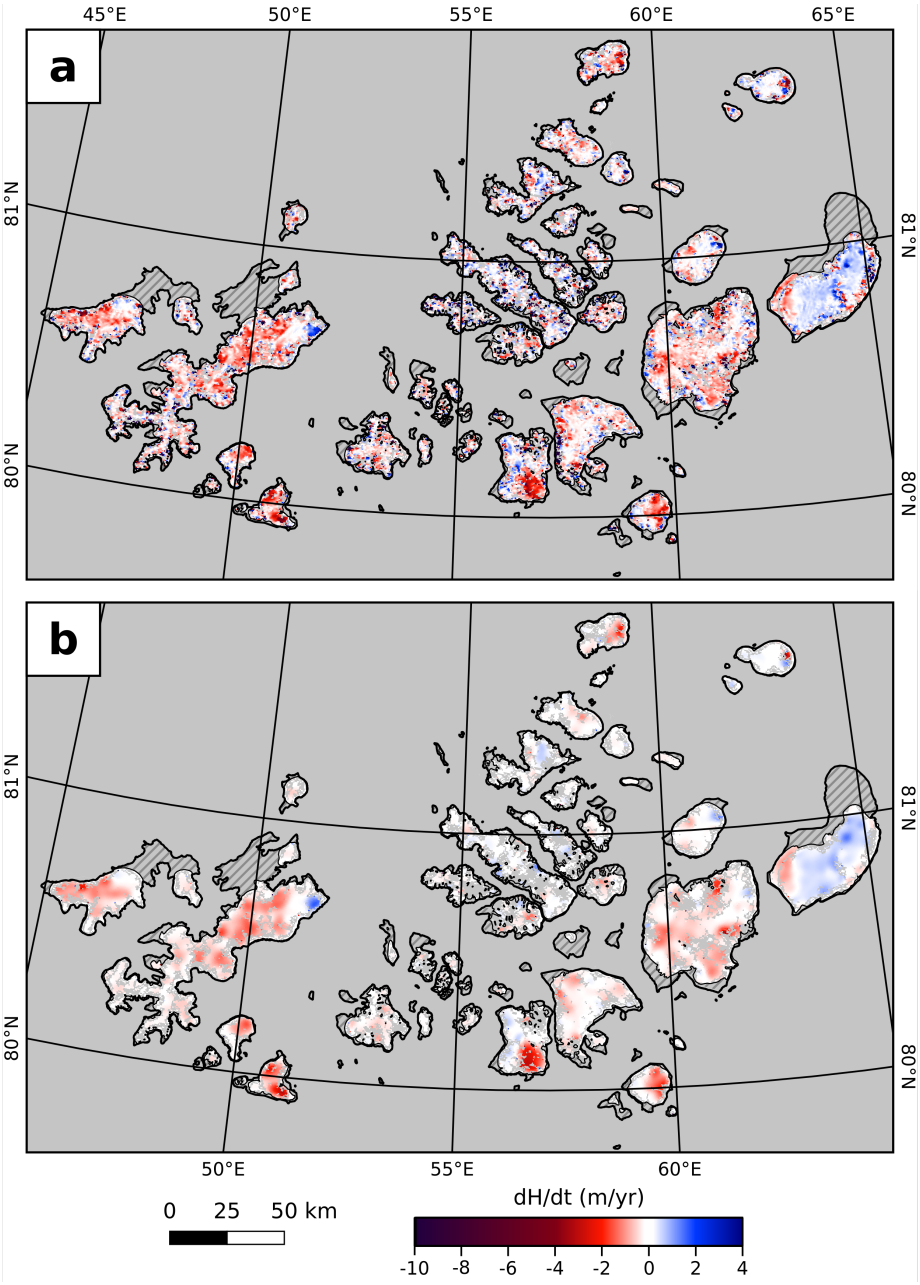

Figure 9: CryoSat-2 $\frac{dh}{dt}$ between June 1, 2011 to October 1, 2015, clipped with the RGI glacier outline. (a) The raw $\frac{dh}{dt}$ map. (b) The masked and Gaussian-filtered $\frac{dh}{dt}$ with T_1 of 2.2 and T_2 of 3.2 (Figure 10).

4.3. Comparison between WorldView and CryoSat-2 $\frac{dh}{dt}$

The correlation coefficient between pre-masked CryoSat-2 $\frac{dh}{dt}$ map (Figure 9a) and WorldView $\frac{dh}{dt}$ map (Figure 7b, warped into the same spatial resolution as well) is 0.082 calculated from 24,634 overlapped pixels over glacierized area. When both masking thresholds T_1 and T_2 decrease, the correlation coefficient between masked points and the WorldView $\frac{dh}{dt}$ increases, and the fitted slope is closer to 1 (that is, CryoSat $\frac{dh}{dt}$ is closer to WorldView $\frac{dh}{dt}$), while less pixels remain (Figure S7). Figure 9b shows an example where T_1 and T_2 are 2.2 and 3.2 respectively, and a Gaussian filter with a standard deviation of 3 and a radius of 5 pixels was applied for better smoothing. In the selected example, the correlation coefficient between masked CryoSat-2 $\frac{dh}{dt}$ and WorldView $\frac{dh}{dt}$ increases to 0.35 using 19,640 overlapped pixels (79.7% of total overlapped pixels). The increased correlation and the cell-by-cell density scatter plots between CryoSat-2 $\frac{dh}{dt}$ and WorldView $\frac{dh}{dt}$ (Figure 10) both indicate that our methodology has successfully masked CryoSat $\frac{dh}{dt}$. Thus, a similar pattern of elevation changes across FJL (Figure 9b) can be recognized from both datasets. Note that the vertical trend in Figure 10b suggests that WorldView $\frac{dh}{dt}$ may have other errors, for example, due to insufficient elevations for regression (See section 5.3).

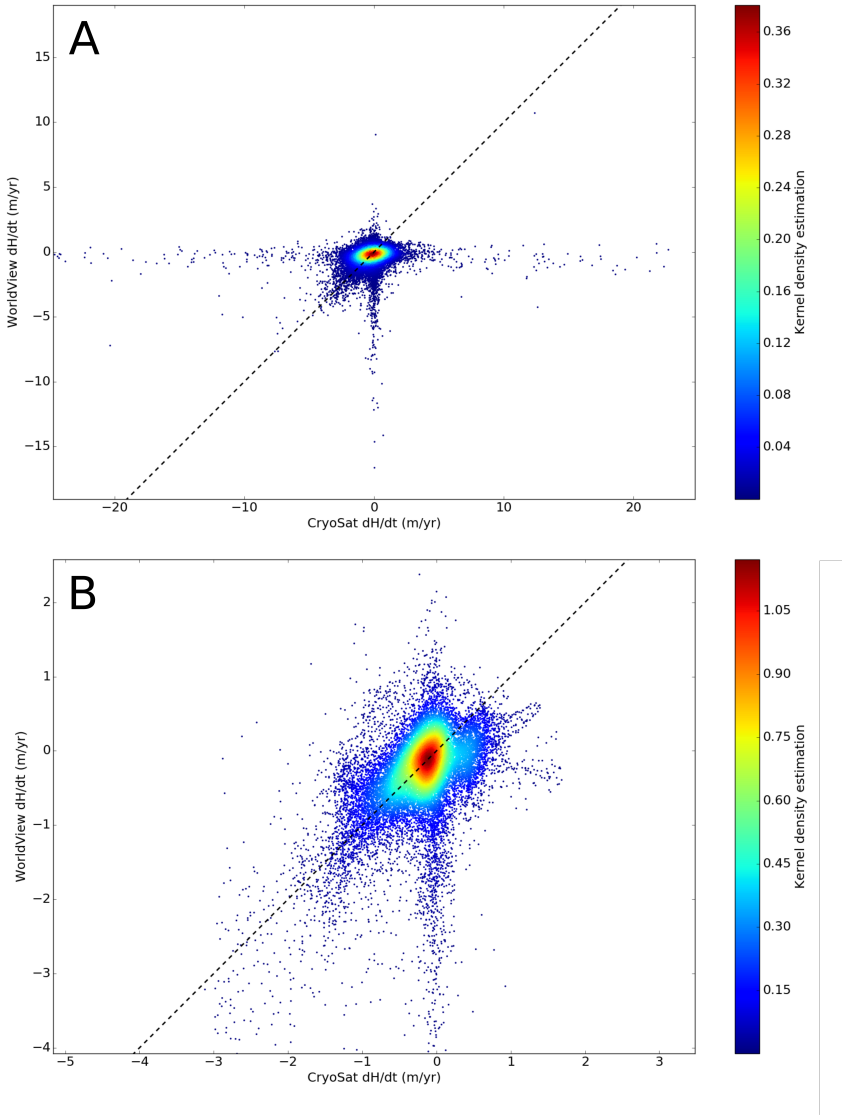

Figure 10: Density scatter plot between WorldView and CryoSat $\frac{dh}{dt}$ using Gaussian kernels for the the estimate of the probability density function. (a) The raw, unmasked CryoSat $\frac{dh}{dt}$. (b) The masked CryoSat $\frac{dh}{dt}$ using $T_1 = 2.2$ and $T_2 = 3.2$. Note the difference of scale in both panels, and that the raw CryoSat $\frac{dh}{dt}$ is highly variable relative to WorldView $\frac{dh}{dt}$. The dashed line indicates the 1:1 ratio of WorldView and CryoSat data.

5. Discussion

5.1. The Acceleration of Ice Loss During 1953-2015

Macheret et al. (1999) reported that the ice volume loss at FJL between 1953 and 1993 was 41.9 km^3 using the same cartographic source in 1953 and airborne radio-echo sounding in 1994; that is, ice mass change rate is -0.89 Gt yr^{-1} using our assumed ice density. It is concluded by Sharov (2010) that the rate of ice loss on FJL derived from ERS-1/2 differential interferometry, ICESat and cartographic elevations has increased by 20% between the 1950s and the 2000s. Since our estimated mass loss between 1953 and 2011-2013 is higher than the estimates between 1953-1994 or 1953-2000s, it is likely that the rate of ice loss has further increased in the 2000s, resulting in a more negative annual balance than the average over the past 60 years. During the 2000s, Moholdt et al. (2012) obtained an ice budget of -0.9 ± 0.7 Gt yr^{-1} using ICESat in 2004-2009; several studies also use GRACE for the estimate of ice budget, e.g. Moholdt et al. (2012) (0.7 ± 3.5 Gt yr^{-1} in 2004-2009; 0.1 ± 3.4 Gt yr^{-1} in 2003-2010), Matsuo & Heki (2013) (-0.8 ± 1.3 Gt yr^{-1} in 2004-2012; -3.5 ± 1.9 Gt yr^{-1} in 2004-2008), Root et al. (2015) (-1.9 ± 0.6 Gt yr^{-1} in 2003-2013), and Jacob et al. (2012) (0 ± 2 Gt yr^{-1} in 2003-2010).

One complication to the interpretation that the mass loss is increasing with time is that mass loss between 2004-2009 from ICESat is several times lower than the 60 year average; that is, -0.9 ± 0.7 Gt yr^{-1} (from Moholdt et al. (2012)) compared to -2.18 ± 0.72 Gt yr^{-1}. A possible reason responsible for the difference may come from the spatial sampling of ICESat. The distance between two parallel ICESat tracks is typically 5-15 km, and thus ICESat may not capture the thinning signal from small-sized glaciers; for example, the most rapidly thinning glacier at Salm Island in 2013-14 is only 4 km wide and 10 km long. Thus, ICESat returns cannot resolve the thinning signal well (see Moholdt et al. (2012) or Figure S1), and underestimates the actual changes of ice mass, especially when $\frac{dh}{dt}$ is fitted to elevations with a third-order polynomial as used by Moholdt et al. (2010b, 2012). To test this hypothesis, we use $\frac{dh}{dt}$ values from

our results but only select those at ICESat track locations. Then we fit $\frac{dh}{dt}$ to elevations using a third-order polynomial, the same method used to calculate ice mass loss in Moholdt et al. (2012) and Moholdt et al. (2010b). The test result shows that the incomplete sampling by ICESat underestimates the mass loss across the archipelago by about 10%, which is enough of an effect for our mass loss estimate to overlap with the ICESat result within error. The details of the test are available in Supplementary Text S1.

The ice loss rate from WorldView DEMs between 2011 and 2015 doubles the long-term rate between 1953 and 2011/2015, and is more negative than any studies that use ICESat or GRACE. This suggests that FJL is losing ice more rapidly compared to previous decades. Although spatially variable, fast-thinning glaciers are spread widely across FJL (Figure 11c-h) and the maximum ice thinning has reached -10 m yr^{-1} at a few outlet glaciers (e.g. Figure 11e, at Wilczek Land). Glaciers that thinned the most rapidly between 1953 and 2011/2015 are still thinning, but many more glaciers have started to thin recently and the fastest thinning rates occurring at present manifest at these newly thinning glaciers. In southeastern FJL, where ice velocity data are available from Strozzi et al. (2017), fast-thinning glaciers correspond to regions with increased glacier frontal speed between 1998 and 2016, derived from JERS-1 and Sentinel-1 SAR data respectively. This suggests that terminus dynamics may play a major role in controlling glacier thinning (e.g., Moholdt et al., 2010a; Dowdeswell et al., 2008), in addition to simple changes in surface mass balance.

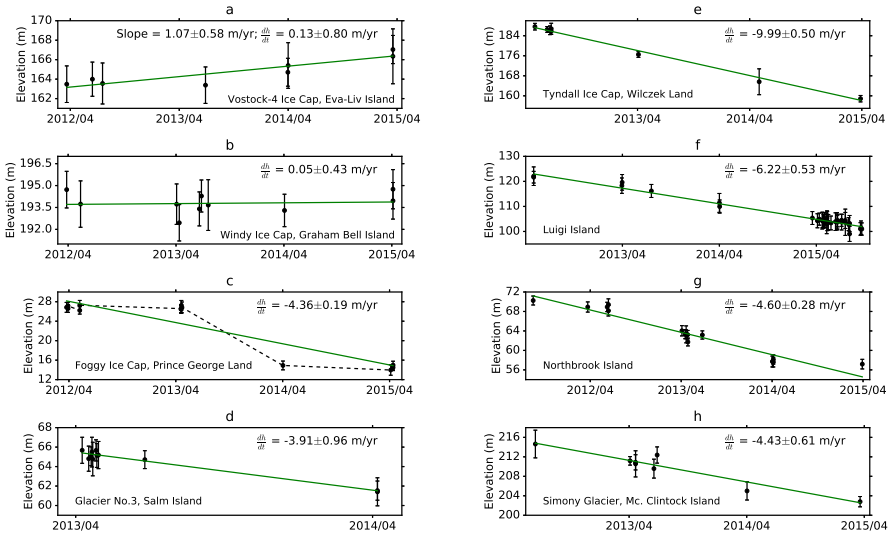

Figure 11: Examples of glacier elevation change from the WorldView linear regression (2011-2015). The location for each time series is labeled in Figure 7. Note that at Vostock-4 Ice Cap in Eva-Liv Island (subpanel a), $\frac{dh}{dt}$ is corrected by the average off-ice value. In addition, the changes in subpanel c (Foggy Ice Cap in Prince George Land) show that ice has retreated and the elevation reached sea level (14 m above the ellipsoid) between 2013 and 2014.

5.2. Case Study: Salm Island

With the 2007 SPOT-5 DEM available in southeastern FJL, the ice-cap drainage basins at Salm Island (Figure 12) provide examples of accelerating thinning. The average $\frac{dh}{dt}$ at this island between 1953 and 2007 is -0.097 ± 0.348 m yr^{-1}. While this average thinning is not significant due to a large uncertainty, the major thinning glacier located in the northern part of the island where thinning peaks at up to -1.26 ± 0.35 m yr^{-1} suggests the existence of thinning glaciers. Between 2007-2013, the average $\frac{dh}{dt}$ is -0.263 ± 0.626 m yr^{-1}, which is 2.7 times higher than the previous 54-year average. Although the average ice thinning rate is still within its uncertainty, the fastest thinning region, now shifted from the northern part of the island to the eastern side, had a doubled maximum thinning rate at -2.60 ± 0.85 m yr^{-1}. Between 2013 and 2014, the average $\frac{dh}{dt}$ on Salm Island increased in magnitude to -1.034 ± 0.077 m yr^{-1}, which is 3.9 times higher than the 2007-2013 average rate.

It is clear that the glacier on the east side of Salm Island (Glacier No. 3 in Sharov (2008)) has experienced accelerating thinning. The $\frac{dh}{dt}$ value at the sample pixel in Figure 12 (time series shown in Figure 11d) changed from -0.389 ± 0.348 m yr^{-1} (1953-2007) to -1.58 ± 0.71 m yr^{-1} (2007-2013), and further increased into -3.91 ± 0.96 m yr^{-1} (2013-2014), making this glacier the fastest-thinning glacier on Salm Island and the 6th fastest thinning glacier in FJL during the WorldView time span.

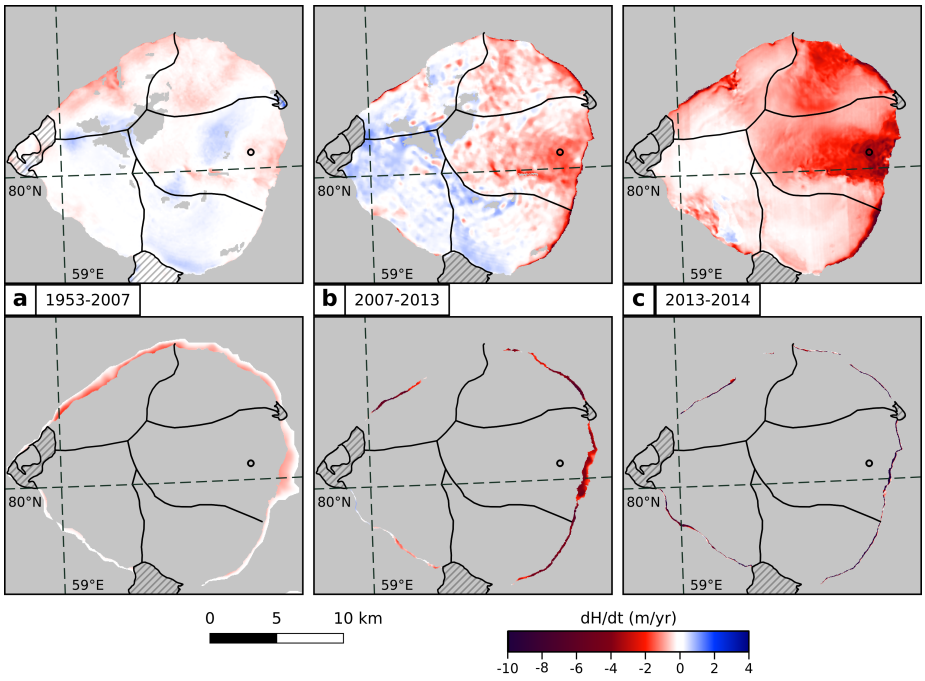

Figure 12: $\frac{dh}{dt}$ map of Salm Island. (a) 1953-2007 (cartographic map to SPOT-5); (b) 2007-2013 (SPOT-5 to WorldView); (c) 2013-2014 (WorldView). Upper panels shows surface elevation changes; lower panels shows where elevation changes are caused by retreat or advance. The average $\frac{dh}{dt}$ for the whole island, including both types of elevation changes, is -0.097 ± 0.348, -0.263 ± 0.626, and -1.034 ± 0.077 m yr^{-1} for the three time periods. Ice cap drainage basins are drawn by black lines, and hatching indicates ice-free areas. Small open circle on the most rapidly thinning ice is the sample location of the time series in Figure 11d.

5.3. Spatial Patterns of Ice Mass Changes

To determine if a spatial pattern in thinning is a true signal or an error from DEM artifacts, we can simply compare it to the glacier topography. For example, the glacier #5 at Wilczek Land (Figure 13) exhibits some thickening (blue) areas that are not correlated to either topography or glacier outlines, thus they are interpreted as patterns most likely related to DEM artifacts. On the other hand, thinning patterns at glacier #2, #10, and #13 are confined by glacier side walls or by a low-slope area, suggesting that the thinning may be related to glacier dynamics. We examine all the rapidly thinning glaciers based on this criterion and rule out suspicious areas when analyzing the thinning trend across FJL.

A trend towards increasing glacier and ice cap thinning from the northeast to the southwest across FJL is apparent in our results in both time spans (Figure 7), consistent with the findings of Sharov (2010) and Moholdt et al. (2012). Most rapidly thinning glaciers are located in the south and west. Nearly all outlet glaciers have thinned at 1-5 m yr^{-1} in the western segment of Prince George Land (Peary Ice Cap) between 2011 and 2015, while the Vostock-4 Ice Cap and Windy Ice Cap at the eastern side of FJL show a neutral rate around 0 m yr^{-1} (Figure 11a-b). Windy Ice Cap is particularly intriguing as it had widespread thickening of 0-1 m yr^{-1} with an error estimate around 0.31 yr^{-1} between 1953 and 2011/15, and a similar value also observed between 1953-2008 and 2004-2009 (Sharov, 2010; Moholdt et al., 2012); however, ice balance changed to a neutral rate (i.e. insignificant thickening) between 2011 and 2015 (Figure 7 11b). Windy Ice Cap thus becomes the largest ice cap that shows a possible recent sign change from thickening to thinning on FJL. Continued observations are required to determine if such a transition to thinning is permanent or if this is a short lived event.

Consistent with previous work (e.g., Sharov, 2010; Moholdt et al., 2012), we find that adjacent glaciers on FJL can have radically different behavior. For example, a sample pixel at a thinning glacier in eastern Wilczek Land, labeled 4e in Figure 7, with the time series in Figure 11e, and as glacier #2 in Figure

13, has accelerated from neutral -0.03 ± 0.31 m yr^{-1} (1953-2012) to -9.99 ± 0.25 m yr^{-1} (2012-2015). This is the most rapidly thinning glacier observed between 2012 and 2015. The adjacent Renown Glacier immediately to the south (glacier #1 in Figure S18), with a larger catchment, was thinning at a maximum rate of -2.5 m yr^{-1} in 1953-2010; however, the maximum thinning rate at the same place reduced to around -1 m yr^{-1} in 2011-2015. That adjacent glaciers behave so differently suggests the presence of slow collapse events and the increased velocity of ice flow controlled by ice dynamics (e.g., Rinne et al., 2011).

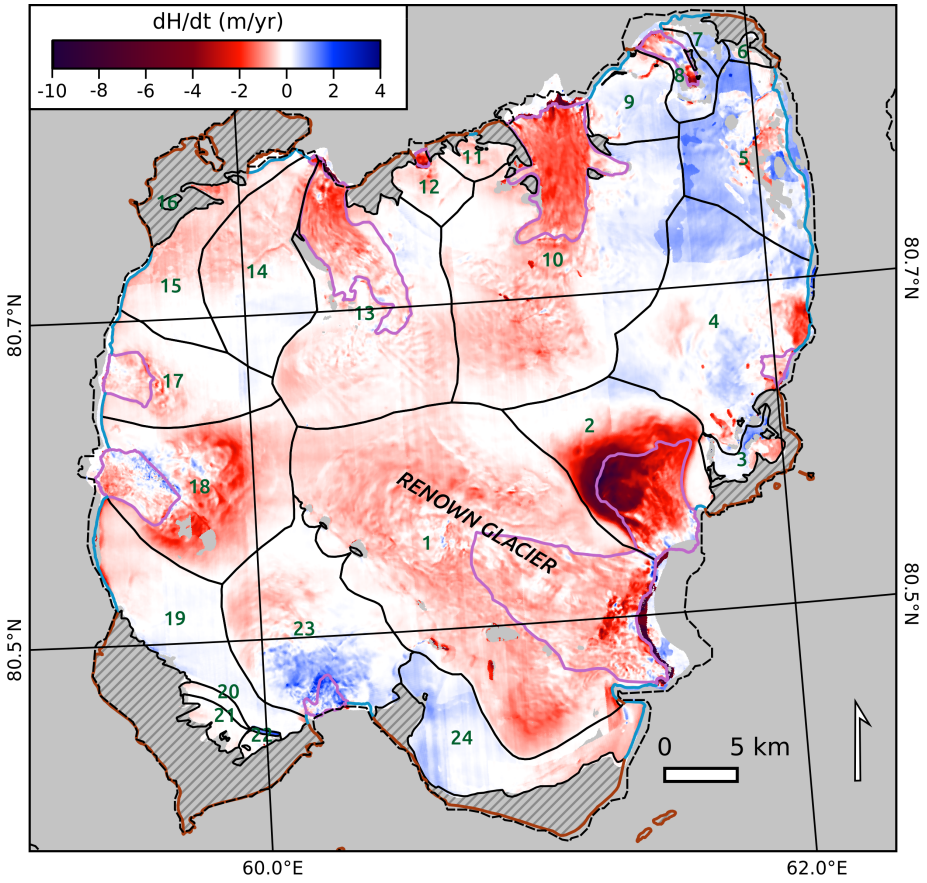

Figure 13: Detailed $\frac{dh}{dt}$ map at Tyndall Ice Cap, Wilczek Land, in 2011-15. Each ice catchment basin outlined by black lines is labeled from 1 to 24 respectively. Brown and blue lines are the off-ice and ice coastline in 2011-15 respectively, mapped using WorldView DEMs and Landsat imagery. Pink areas are glacier outlets that have a relatively low slope to the surrounding ice. The coastlines in 1953 are shown as black dashed lines, and off-ice land surface is shown as hatched region. The location of this figure is shown in Figure 7.

5.4. Changes of ice outline and glacier termini

The glacierized area of Franz Josef Land has reduced by over 200 km^2 since 1953 (Macheret et al., 1999; Helm, 2007; Sharov, 2010), and the ice margin retreat is ongoing, as recognized using Landsat imagery from 2017. Rapid ice retreat in FJL occurs primarily at marine-terminating ice cap boundaries, whereas land-terminating ice caps shrink at much slower rates (negligible in the time span of 2011-2015). This suggests that ocean warming and/or the reduction of sea ice concentration (SIC) likely exert an important control on the glacier dynamics of the archipelago (e.g., Carr et al., 2017).

Figure 11c shows a typical retreat of a marine ice margin revealed by the elevation time series. The glacier is located within a coastal bay on the southeastern side of Prince George Land (Figure 1 and 7). The ice retreat occurs at the marine front with a low surface gradient which is proposed by Dowdeswell et al. (1994) as a possible ice shelf. In 2012, the ice surface was 13-m above sea level (27 m above the ellipsoid). Between April 2013 and April 2014 the ice calved away. The glacier's marine terminus retreated 200-500 m between 2012 and 2015, roughly equal to about 30% of the proposed ice-shelf area. The average $\frac{dh}{dt}$ between 2012 and 2015 was -4.36 ± 0.10 m yr^{-1}, but this value is clearly an under-estimate of the rapid $\frac{dh}{dt}$ changes that all occurred between April 2013 and 2014. This illustrates that rapid changes in $\frac{dh}{dt}$ at the marine termini of FJL ice caps are recording margin retreat by calving when elevations approach sea level.

In addition, retreat of marine-terminating glaciers is observed regardless of elevation changes in ice cap interiors; for example, the margin of the Vostock-4 Ice Cap has retreated around 150 m within 3 years (2012-2015) but $\frac{dh}{dt}$ is stable in its interior (Figure 11a 14). However, this is the exception rather than the rule. At the terminus of most rapid-thinning glaciers, including those with suspected floating ice shelves, ice front retreat is occurring at the fastest rates observed across FJL. The terminus of Renown Glacier, Wilczek Land, with a possible ice-shelf margin (Dowdeswell et al., 1994, 2010; Dowdeswell, 2017), has retreated at a speed of 325 m yr^{-1} between 2012 and 2014. Dowdeswell et al.

(2010) reported that the same margin has retreated at around 90 m yr^{-1} within 45 years. It is thus likely that the retreat of the marine ice boundary in many places has also accelerated over past decades. A similar trend has also been reported elsewhere in the Atlantic Arctic (Carr et al., 2017).

Renown Glacier provides an example of how much ice mass loss can be contributed from frontal retreat and from iceberg production. A simple calculation shows that calving mass loss from here alone may be on the order of 0.2 Gt yr^{-1} (8 km width $\times$ 0.1 km thickness (Sharov, 2010) $\times$ the summation of glacier retreat and glacier speed of 0.3 km yr^{-1} (Strozzi et al., 2017)). In our $\frac{dh}{dt}$ measurement, we recognize frontal retreat as part of a thinning pattern across the archipelago (e.g. Figure 11c) and calculate the average $\frac{dh}{dt}$ during a given time period to estimate ice loss. However, since our $\frac{dh}{dt}$ measurement does not take ice mass that is below the water level into account, it therefore presents a conservative estimate of total mass loss from FJL. The total volume change rate $\frac{dV}{dt}$ consists of the surface mass balance (e.g. surface melting, snow accumulation) and the ice calving flux (Nuth et al., 2012). Our results cannot determine how much both factors account for because we do not analyze the margin retreat and ice velocity, but studies from marine-terminating ice caps in Severnaya Zemlya and eastern Svalbard show that ice calving flux represents $30 - 40\%$ of the total volume change rate (Dowdeswell et al., 2002, 2008).

Ice retreat has also resulted in the formation of a new island in the southeast of Hall Island (Sharov & Nikolskiy, 2017; Pelto, 2018). In 2002 the new island was still a peninsula with an area of 59.5 km^2, connected to Hall Island by marine-terminating glaciers (Figure S9). Landsat 8 imagery shows that in the summer of 2013, the glacier front at Hall Island disintegrated, leaving only a narrow ice bridge connecting to the new island. In the summer of 2016, the ice bridge broke, and the new island became separate from Hall Island. Imagery from 2017 indicates that the ice front has not re-advanced. Such an island-forming process has been reported from the neighboring island of Spitsbergen (Burton et al., 2016) and from around the coastal region of Greenland (e.g., van As, 2011; Rudolf, 2007), and a new island was reported and recently confirmed

in FJL due to the detachment of the tombolo (Barr, 2016) at Northbrook Island.
670 Nevertheless, this is the first time that a new island due to glacier retreat has been observed in the archipelago using remotely sensed data. It is expected that further islands will emerge in FJL, as ice losses have reached an unprecedented rate since measurements began.

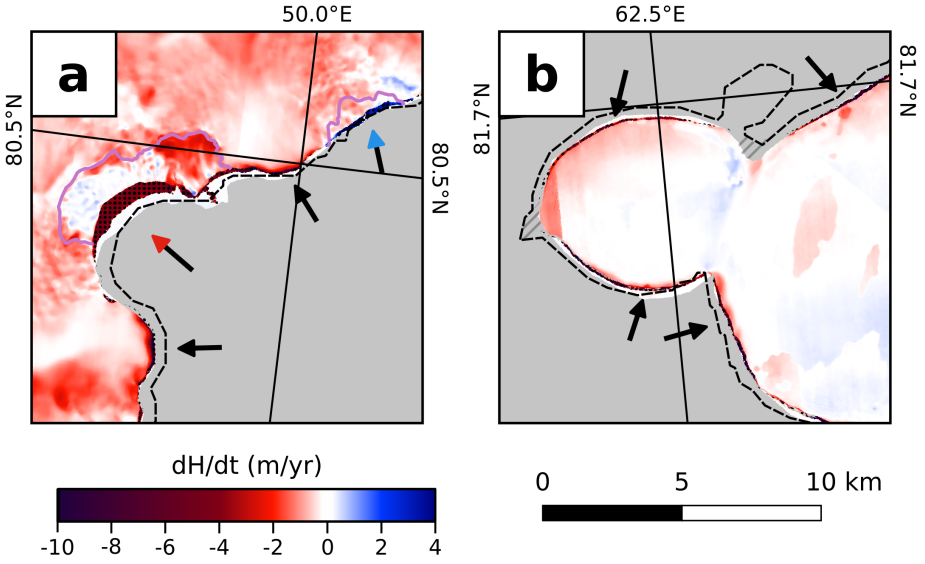

Figure 14: The changes of glacier fronts at (a) Prince George Land and (b) Vostock-4 Ice Cap in 2011-15, as dark rims indicated by dotted pattern and arrows, generally shows a low $\frac{dh}{dt}$ value at -6 to -10 m yr^{-1} and is independent of the parent ice cap's current ice budget. The red arrow points to an ice front at low surface gradient (bound by the purple line), where ice has retreated more than other places shown in this figure. The blue arrow points to one of a few places in FJL where ice front has slightly advanced in this time span. Black dashed lines label the coastlines in 1953, mapped using the cartographic DEM. Ice-free land surface is shown as striped region. The location of this figure is shown in Figure 7.

5.5. A Potential Link to the Warming of the Arctic

The warming of the Arctic (e.g., Screen & Simmonds, 2010; Pithan & Mauritsen, 2014) is likely responsible for the increased ice loss in FJL since the 2000s. Since ice retreating and glacier thinning primarily took place at marine terminating glaciers during the recent decades, we compare the SST and SIC data to the changes of ice budget from 1953 to 2015 (Figure 15). Unfortunately, SST and SIC data are released in one-degree grids, that makes the comparison with the spatial $\frac{dh}{dt}$ patterns hard to achieve. Here we focus on the temporal changes of both datasets, and use the average value across the FJL for temporal comparison. The summer SST at FJL was bounded between ± 0.7°C between 1953 and 2005, but it started to increase from 0.5°C in 2005 to 1.9°C in 2010 (Hirahara et al., 2014). The time series of SIC also shows that, during 2000-2010, winter SIC decreased by about 10% and summer SIC decreased by about 50%. In the summer of 2009, sea ice was nearly absent around FJL for the first time on record (Hirahara et al., 2014). These changes in the late 2000s suggest that ice loss from FJL is probably driven by a combination of surface-melting and runoff together with enhanced ablation of marine-terminating glacier fronts. Marine-terminating glaciers are susceptible to accelerating ice losses by iceberg calving as the ocean warms (e.g., Carr et al., 2017).

The higher rate of ice loss during 2011-15 is also likely due to the effects of warming ocean temperatures on marine-terminating glaciers. The summer SSTs between 2011 and 2015, were all more than 0.8°C (more than the maximum summer SST between 1953 and 2005) except for 2014 (0.5°C) (Hirahara et al., 2014). Summer SICs were also all below 45% (except for 2014 at 75%), in contrast to the average of 69% between 1953-2010 (Hirahara et al., 2014). In 2016, summer SIC reached its record low at 29%, which may have lead to the break up of the ice bridge in the southeast of Hall Island (see section 5.4). The following winter SIC in 2016/17 also dropped to 71% compared to a typical range between $80 - 90$% before 2011. Assuming continued warming of the Arctic, it is possible that surface melt would increase over time; however, given that a portion of ice loss was due to the dynamic change of the ice front, it is unclear

705 if ice loss may continue to accelerate over the coming decades as we are not sure how long the glaciers at FJL can sustain a prolonged frontal retreat. For example, a marine terminating ice cap may eventually terminate on land due to the ice retreat, which can lead to a significant decrease of ice calving flux.

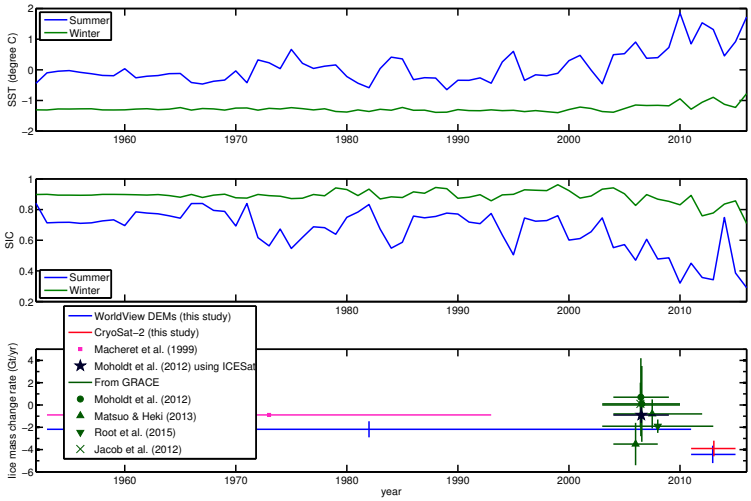

Figure 15: The time series of SST (upper panel) and SIC (middle panel). The green line shows the winter average and the blue line shows the summer average. The lower panel is the change of the average $\frac{dh}{dt}$ between 1953 and 2015 from different studies. and approaches. Horizontal bars indicate the time span of each estimate, and vertical bars are errors at 95% confidence. Note that there is no error reported from Macheret et al. (1999).

6. Conclusions

This study provides strong evidence from satellite-derived and cartographic DEMs that FJL had a negative ice mass balance between 1953 and 2011/15. The ice mass loss rate between 2011 and 2015 was -4.43 ± 0.78 Gt yr^{-1} which doubled the long term rate (-2.18 ± 0.72 Gt yr^{-1}) between 1953 and 2011/15. The absolute values for mass loss are a conservative measure of total mass loss from FJL, since our approach does not include ice loss below the water surface due to ice calving. Based on the analysis of $\frac{dh}{dt}$ from WorldView, CryoSat-2, SPOT-5, as well as studies that focus on changes in the 2000s using ICESat and GRACE, it is likely that the loss of ice mass has accelerated since late 2000s. Elevation change rates across the archipelago are spatially variable, but more glaciers are thinning at higher rates of up to 10 m yr^{-1} in this recent decade, compared to the 60-yr average. The change of the ice loss rate suggests that anomalies of SST and SIC have possibly disrupted the previously almost neutral glacier mass balance of FJL, yielding a more negative ice budget which more closely resembles the neighboring archipelagos of Svalbard and Novaya Zemlya. The focus of loss at marine terminating ice caps suggests that observed ocean temperature changes play an important role, similar to those archipelagos. A SW-NE thinning-thickening pattern over FJL is mapped, likely linked to warmer climate conditions in the southwest. Most marine terminating ice fronts have been retreating for over 60 years, and glacier retreat generated a new island in 2016.

Acknowledgments

This work was partly supported by NASA grants NNX11AR14G and NNX12AO31G. WorldView, QuickBird 2 and GeoEye-1 imagery was provided by the Polar Geospatial Center at the University of Minnesota, which is supported by NSF OPP awards 1043681 and 1559691. Worldview DEMs used in this work were created from DigitalGlobe, Inc. imagery. DEMs from ArcticDEM project were provided by the Polar Geospatial Center under NSF OPP awards

1043681, 1559691 and 1542736. Landsat data are downloaded via the USGS tool EarthExplorer. COBE-SST2 data were provided by the NOAA/OAR/ESRL Physical Sciences Division. The CryoSat work was performed under the European Space Agency (ESA) Support to Science Elements CryoSat+ CryoTop contract 4000107394/12/I-NB, CS+ Mountain Glaciers contract 4000114224/15/I-SBo. ICESat data were generously provided by Dr. Geir Moholdt of the Norwegian Polar Institute. We thank the University of North Carolina at Chapel Hill Research Computing group for providing computational resources that have contributed to these research results. Whyjay Zheng acknowledges the support from the Overseas Ph.D. Scholarship granted by Ministry of Education, Taiwan.

References

van As, D. (2011). Warming, glacier melt and surface energy budget from weather station observations in the melville bay region of northwest greenland. *Journal of Glaciology*, *57*, 208–220. doi:10.3189/002214311796405898.

Barr, S. (1995). *Franz Josef Land*. Oslo: Norwegian Polar Institute.

Barr, W. (2016). A new island in Zemlya Frantsa-Iosifa [Franz Josef Land]. *Polar Record*, *52*, 372–373. doi:10.1017/S0032247415000807.

Beyer, R. A., Alexandrov, O., & Moratto, Z. (2014). Aligning terrain model and laser altimeter point clouds with the Ames Stereo Pipeline. In *45th Lunar and Planetary Science Conference (Abstract 2902)*.

Burton, D. J., Dowdeswell, J. A., Hogan, K. A., & Noormets, R. (2016). Marginal Fluctuations of a Svalbard Surge-Type Tidewater Glacier, Blomstrandbreen, Since the Little Ice Age: A Record of Three Surges. *Arctic, Antarctic, and Alpine Research*, *48*, 411–426. doi:10.1657/AAAR0014-094.

Carabajal, C. C., & Harding, D. J. (2005). ICESat validation of SRTM C-band digital elevation models. *Geophysical Research Letters*, *32*, L22S01. doi:10.1029/2005GL023957.

Carr, J. R., Stokes, C. R., & Vieli, A. (2017). Threefold increase in marine-terminating outlet glacier retreat rates across the Atlantic Arctic: 1992-2010. *Annals of Glaciology*, (pp. 1–20). doi:10.1017/aog.2017.3.

Cohen, J., Screen, J. A., Furtado, J. C., Barlow, M., Whittleston, D., Coumou, D., Francis, J., Dethloff, K., Entekhabi, D., Overland, J., & Jones, J. (2014). Recent Arctic amplification and extreme mid-latitude weather. *Nature Geoscience*, *7*, 627–637. doi:10.1038/ngeo2234.

Dowdeswell, J. A. (2017). Arctic Ice Shelves and Ice Islands. In L. Copland, & D. Mueller (Eds.), *Arctic Ice Shelves and Ice Islands* chapter 3. (pp. 55–74). Springer Netherlands. (1st ed.). doi:10.1007/978-94-024-1101-0.

Dowdeswell, J. A., Bassford, R. P., Gorman, M. R., Williams, M., Glazovsky, A. F., Macheret, Y. Y., Shepherd, A. P., Vasilenko, Y. V., Savatyuguin, L. M., Hubberten, H. W., & Miller, H. (2002). Form and flow of the Academy of Sciences Ice Cap, Severnaya Zemlya, Russian High Arctic. *Journal of Geophysical Research: Solid Earth*, *107*, EPM 5–1–EPM 5–15. doi:10.1029/2000JB000129.

Dowdeswell, J. A., Benham, T. J., Strozzi, T., & Hagen, J. O. (2008). Iceberg calving flux and mass balance of the Austfonna ice cap on Nordaustlandet, Svalbard. *Journal of Geophysical Research: Earth Surface*, *113*, F03022. doi:10.1029/2007JF000905.

Dowdeswell, J. A., Dowdeswell, E. K., Williams, M. W., & Glazovsky, A. F. (2010). The glaciology of the Russian High Arctic from Landsat imagery. In R. S. Williams Jr, & J. G. Ferrigno (Eds.), *US Geological Survey Professional Paper* (pp. 94–125). U.S. Geological Survey volume 1386-F. URL: http://pubs.usgs.gov/pp/p1386f/pdf/Asia_front_pgs.pdf.

Dowdeswell, J. A., Gorman, M. R., Glazovsky, A. F., & Macheret, Y. Y. (1994). Evidence for Floating Ice Shelves in Franz Josef Land, Russian High Arctic. *Arctic and Alpine Research*, *26*, 86–92. doi:10.2307/1551882.

Dowdeswell, J. A., & Williams, M. (1997). Surge-type glaciers in the Russian High Arctic identified from digital satellite imagery. *Journal of Glaciology*, *43*, 489–494. doi:10.3189/S0022143000035097.

Durkin, W. J., Bartholomaus, T. C., Willis, M. J., & Pritchard, M. E. (2017). Dynamic Changes at Yahtse Glacier, the Most Rapidly Advancing Tidewater Glacier in Alaska. *Frontiers in Earth Science*, *5:21*. doi:10.3389/feart.2017.00021.

Fahnestock, M., Scambos, T., Moon, T., Gardner, A., Haran, T., & Klinger, M. (2016). Rapid large-area mapping of ice flow using Landsat 8. *Remote Sensing of Environment*, *185*, 84–94. doi:10.1016/j.rse.2015.11.023.

de Ferranti, J. (2014). Digital Elevation Data - with SRTM voids filled using accurate topographic mapping. URL: http://www.viewfinderpanoramas.org/dem3.html.

Foresta, L., Gourmelen, N., Pálsson, F., Nienow, P., Björnsson, H., & Shepherd, A. (2016). Surface elevation change and mass balance of Icelandic ice caps derived from swath mode CryoSat-2 altimetry. *Geophysical Research Letters*, *43*, 12,138–12,145. doi:10.1002/2016GL071485.

Forman, S. L., Lubinski, D. J., Ingólfsson, Ó., Zeeberg, J. J., Snyder, J. A., Siegert, M. J., & Matishov, G. G. (2004). A review of postglacial emergence on Svalbard, Franz Josef Land and Novaya Zemlya, northern Eurasia. *Quaternary Science Reviews*, *23*, 1391–1434. doi:10.1016/j.quascirev.2003.12.007.

Fricker, H. A., Borsa, A., Minster, B., Carabajal, C., Quinn, K., & Bills, B. (2005). Assessment of ICESat performance at the salar de Uyuni, Bolivia. *Geophysical Research Letters*, *32*, L21S06. doi:10.1029/2005GL023423.

Gardner, A. S., Moholdt, G., Cogley, J. G., Wouters, B., Arendt, A. A., Wahr, J., Berthier, E., Hock, R., Pfeffer, W. T., Kaser, G., Ligtenberg, S. R. M., Bolch, T., Sharp, M. J., Hagen, J. O., van den Broeke, M. R., & Paul, F.

(2013). A Reconciled Estimate of Glacier Contributions to Sea Level Rise: 2003 to 2009. *Science*, *340*, 852–857. doi:10.1126/science.1234532.

Gourmelen, N., Escorihuela, M. J., Shepherd, A., Foresta, L., Muir, A., Garcia-Mondejar, A., Roca, M., Baker, S., & Drinkwater, M. R. (2017a). CryoSat-2 swath interpherometric altimetry for mapping ice elevation and elevation change. *Advances in Space Research*, *in press*. doi:10.1016/j.asr.2017.11.014.

Gourmelen, N., Goldberg, D. N., Snow, K., Henley, S. F., Bingham, R. G., Kimura, S., Hogg, A. E., Shepherd, A., Mouginot, J., Lenaerts, J. T., Ligtenberg, S. R., & van de Berg, W. J. (2017b). Channelized Melting Drives Thinning Under a Rapidly Melting Antarctic Ice Shelf. *Geophysical Research Letters*, *44*, 9796–9804. doi:10.1002/2017GL074929.

Grant, K. L., Stokes, C. R., & Evans, I. S. (2009). Identification and characteristics of surge-type glaciers on Novaya Zemlya, Russian Arctic. *Journal of Glaciology*, *55*, 960–972. doi:10.3189/002214309790794940.

Grosswald, M. G., Krenke, A. N., Vinogradov, O. N., Markin, V. A., Psariova, T. V., Razumeiko, N. G., & Sukhodrovsky, V. L. (1973). *Glaciers of Franz Josef Land: results of research under the programme of the International Geophysical Year*. Moscow: Nauka.

Helm, C. W. (2007). *Glacier Change in Franz Josef Land, 1952-2004*. Master thesis University of Colorado, Denver.

Hirahara, S., Ishii, M., & Fukuda, Y. (2014). Centennial-scale sea surface temperature analysis and its uncertainty. *Journal of Climate*, *27*, 57–75. doi:10.1175/JCLI-D-12-00837.1.

Huss, M. (2013). Density assumptions for converting geodetic glacier volume change to mass change. *The Cryosphere*, *7*, 877–887. URL: http://www.the-cryosphere-discuss.net/7/219/2013/. doi:10.5194/tcd-7-219-2013.

Ismail, Z., & Jaafar, J. (2013). DEM derived from photogrammetric generated DSM using morphological filter. In *2013 IEEE 4th Control and System Graduate Research Colloquium (ICSGRC 2013)* (pp. 103–106). doi:10.1109/ICSGRC.2013.6653284.

Jacob, T., Wahr, J., Pfeffer, W. T., & Swenson, S. (2012). Recent contributions of glaciers and ice caps to sea level rise. *Nature*, *482*, 514–518. doi:10.1038/nature10847.

Jähne, B. (2005). Feature Extraction. In *Digital Image Processing* (pp. 299–446). Berlin; New York: Springer-Verlag Berlin Heidelberg. (6th ed.). doi:10.1007/3-540-27563-0.

Macheret, Y. Y., Glazovsky, A. A. F., Dowdeswell, J. A., & Gorman, M. R. (1999). Ice cap volume change on Franz Josef Land during last 40 years. *Zeitschrift fuer Gletscherkunde und Glazialgeologie*, *35*, 103–116.

Matsuo, K., & Heki, K. (2013). Current ice loss in small glacier systems of the arctic islands (iceland, svalbard, and the russian high arctic) from satellite gravimetry. *Terrestrial, Atmospheric and Oceanic Sciences*, *24*, 657–670. doi:10.3319/TAO.2013.02.22.01(TibXS).

Melkonian, A. K. (2014). *Quantifying and Characterizing Mass Loss From Icefields Using Remote Sensing*. Ph.D. thesis Cornell University.

Melkonian, A. K., Willis, M. J., Pritchard, M. E., Rivera, A., Bown, F., & Bernstein, S. A. (2013). Satellite-derived volume loss rates and glacier speeds for the Cordillera Darwin Icefield, Chile. *Cryosphere*, *7*, 823–839. doi:10.5194/tc-7-823-2013.

Melkonian, A. K., Willis, M. J., Pritchard, M. E., & Stewart, A. J. (2016). Recent changes in glacier velocities and thinning at Novaya Zemlya. *Remote Sensing of Environment*, *174*, 244–257. doi:10.1016/j.rse.2015.11.001.

Moholdt, G., Hagen, J. O., Eiken, T., & Schuler, T. V. (2010a). Geometric changes and mass balance of the Austfonna ice cap, Svalbard. *Cryosphere*, *4*, 21–34. doi:10.5194/tc-4-21-2010.

Moholdt, G., Nuth, C., Hagen, J. O., & Kohler, J. (2010b). Recent elevation changes of Svalbard glaciers derived from ICESat laser altimetry. *Remote Sensing of Environment*, *114*, 2756–2767. doi:10.1016/j.rse.2010.06.008.

Moholdt, G., Wouters, B., & Gardner, A. S. (2012). Recent mass changes of glaciers in the Russian High Arctic. *Geophysical Research Letters*, *39*, L10502. doi:10.1029/2012GL051466.

Moratto, S. Z. M., Broxton, M. J., Beyer, R. A., Lundy, M., & Husmann, K. (2010). Ames Stereo Pipeline, NASA's Open Source Automated Stereogrammetry. In *41st Lunar and Planteary Science Conference (Abstract 2364)*.

Noh, M. J., & Howat, I. M. (2015). Automated stereo-photogrammetric DEM generation at high latitudes: Surface Extraction with TIN-based Search-space Minimization (SETSM) validation and demonstration over glaciated regions. *GIScience & Remote Sensing*, *52*, 198–217. doi:10.1080/15481603.2015.1008621.

Nuth, C., Schuler, T. V., Kohler, J., Altena, B., & Hagen, J. O. (2012). Estimating the long-term calving flux of Kronebreen, Svalbard from geodetic elevation changes and mass-balance modelling. *Journal of Glaciology*, *58*, 119–133. doi:10.3189/2012JoG11J036.

Pelto, M. (2018). Franz Josef Islands Separate due to Glacier Retreat. URL: https://blogs.agu.org/fromaglaciersperspective/2018/01/30/franz-josef-islands-separate-due-glacier-retreat.

Pfeffer, W. T., Arendt, A. A., Bliss, A., Bolch, T., Cogley, J. G., Gardner, A. S., Hagen, J. O., Hock, R., Kaser, G., Kienholz, C., Miles, E. S., Moholdt, G., Mölg, N., Paul, F., Radić, V., Rastner, P., Raup, B. H., Rich, J., Sharp, M. J., Andreassen, L. M., Bajracharya, S., Barrand, N. E., Beedle, M. J., Berthier,

E., Bhambri, R., Brown, I., Burgess, D. O., Burgess, E. W., Cawkwell, F., Chinn, T., Copland, L., Cullen, N. J., Davies, B., De Angelis, H., Fountain, A. G., Frey, H., Giffen, B. A., Glasser, N. F., Gurney, S. D., Hagg, W., Hall, D. K., Haritashya, U. K., Hartmann, G., Herreid, S., Howat, I., Jiskoot, H., Khromova, T. E., Klein, A., Kohler, J., K??nig, M., Kriegel, D., Kutuzov, S., Lavrentiev, I., Le Bris, R., Li, X., Manley, W. F., Mayer, C., Menounos, B., Mercer, A., Mool, P., Negrete, A., Nosenko, G., Nuth, C., Osmonov, A., Pettersson, R., Racoviteanu, A., Ranzi, R., Sarikaya, M. A., Schneider, C., Sigurdsson, O., Sirguey, P., Stokes, C. R., Wheate, R., Wolken, G. J., Wu, L. Z., & Wyatt, F. R. (2014). The randolph glacier inventory: A globally complete inventory of glaciers. *Journal of Glaciology*, *60*, 537–552. doi:10.3189/2014JoG13J176.

Pithan, F., & Mauritsen, T. (2014). Arctic amplification dominated by temperature feedbacks in contemporary climate models. *Nature Geoscience*, *7*, 181–184. doi:10.1038/ngeo2071.

Radić, V., Bliss, A., Beedlow, A. C., Hock, R., Miles, E., & Cogley, J. G. (2014). Regional and global projections of twenty-first century glacier mass changes in response to climate scenarios from global climate models. *Climate Dynamics*, *42*, 37–58. doi:10.1007/s00382-013-1719-7.

Rastner, P., Strozzi, T., & Paul, F. (2017). Fusion of Multi-Source Satellite Data and DEMs to Create a New Glacier Inventory for Novaya Zemlya. *Remote Sensing*, *9*, 1122. doi:10.3390/rs9111122.

Rinne, E. J., Shepherd, A., Palmer, S., van den Broeke, M. R., Muir, A., Ettema, J., & Wingham, D. (2011). On the recent elevation changes at the Flade Isblink Ice Cap, northern Greenland. *Journal of Geophysical Research: Earth Surface*, *116*, F03024. doi:10.1029/2011JF001972.

Root, B. C., Tarasov, L., & van der Wal, W. (2015). GRACE gravity observations constrain Weichselian ice thickness in the Barents Sea. *Geophysical Research Letters*, *42*, 3313–3320. doi:10.1002/2015GL063769.

Rudolf, J. C. (2007). The Warming of Greenland. The New York Times. Accessed September 19, 2017. URL: http://www.nytimes.com/2007/01/16/science/earth/16gree.html.

Screen, J. A., & Simmonds, I. (2010). The central role of diminishing sea ice in recent Arctic temperature amplification. *Nature*, *464*, 1334–1337. doi:10.1038/nature09051.

Serreze, M. C., & Francis, J. A. (2006). The arctic amplification debate. *Climatic Change*, *76*, 241–264. doi:10.1007/s10584-005-9017-y.

Sharov, A., & Nikolskiy, D. (2017). Meltdown of ice bridges and emergence of new islands in the Barents Sea observed by Sentinel-1 INSAR. In *The 10th International Workshop on Advances in the Science and Applications of SAR Interferometry and Sentinel-1 InSAR (FRINGE 2017)*. Helsinki, Finland. doi:10.13140/RG.2.2.12424.62726.

Sharov, A. I. (2008). *Franz Josef Land Region: Glacier changes in 1950-2000s*. Graz, Austria: Joanneum Research. URL: http://dib.joanneum.at/smaragd/downloads/FJL_GCM_500000_130808.pdf.

Sharov, A. I. (2010). *SMARAGD - satellite monitoring and regional analysis of glacier dynamics in the Barents-Kara region, Graz 2010*. Graz, Austria: Joanneum Research. URL: http://dib.joanneum.at/smaragd/downloads/SMARAGD_Brochure_100610_ed_title.pdf.

Shean, D. E., Alexandrov, O., Moratto, Z. M., Smith, B. E., Joughin, I. R., Porter, C., & Morin, P. (2016). An automated, open-source pipeline for mass production of digital elevation models (DEMs) from very-high-resolution commercial stereo satellite imagery. *ISPRS Journal of Photogrammetry and Remote Sensing*, *116*, 101–117. doi:10.1016/j.isprsjprs.2016.03.012.

Shuman, C. A., Zwally, H. J., Schutz, B. E., Brenner, A. C., DiMarzio, J. P., Suchdeo, V. P., & Fricker, H. A. (2006). ICESat Antarctic elevation data:

Preliminary precision and accuracy assessment. *Geophysical Research Letters*, *33*, L07501. doi:10.1029/2005GL025227.

Strozzi, T., Paul, F., Wiesmann, A., Schellenberger, T., & Kääb, A. (2017). Circum-arctic changes in the flow of glaciers and ice caps from satellite SAR data between the 1990s and 2017. *Remote Sensing*, *9*, 947. doi:10.3390/rs9090947.

Sun, Z., Lee, H., Ahn, Y., Aierken, A., Tseng, K. H., Okeowo, M. A., & Shum, C. K. (2017). Recent Glacier Dynamics in the Northern Novaya Zemlya Observed by Multiple Geodetic Techniques. *IEEE Journal of Selected Topics in Applied Earth Observations and Remote Sensing*, *10*, 1290–1302. doi:10.1109/JSTARS.2016.2643568.

Walsh, J. E. (2009). A comparison of Arctic and Antarctic climate change, present and future. *Antarctic Science*, *21*, 179. doi:10.1017/S0954102009001874.

Wang, D., & Kääb, A. (2015). Modeling glacier elevation change from DEM time series. *Remote Sensing*, *7*, 10117–10142. doi:10.3390/rs70810117.

Wessel, P., & Smith, W. H. F. (1996). A global, self-consistent, hierarchical, high-resolution shoreline database. *Journal of Geophysical Research: Solid Earth*, *101*, 8741–8743. doi:10.1029/96JB00104.

Willis, M. J., Melkonian, A. K., & Pritchard, M. E. (2015). Outlet glacier response to the 2012 collapse of the Matusevich Ice Shelf, Severnaya Zemlya, Russian Arctic. *Journal of Geophysical Research: Earth Surface*, *120*, 2040–2055. doi:10.1002/2015JF003544.

Willis, M. J., Melkonian, A. K., Pritchard, M. E., & Ramage, J. M. (2012). Ice loss rates at the Northern Patagonian Icefield derived using a decade of satellite remote sensing. *Remote Sensing of Environment*, *117*, 184–198. doi:10.1016/j.rse.2011.09.017.

Zwally, H. J., Schutz, B., Abdalati, W., Abshire, J., Bentley, C., Brenner, A., Bufton, J., Dezio, J., Hancock, D., Harding, D., Herring, T., Minster, B., Quinn, K., Palm, S., Spinhirne, J., & Thomas, R. (2002). ICESat's laser measurements of polar ice, atmosphere, ocean, and land. *Journal of Geodynamics*, *34*, 405–445. doi:10.1016/S0264-3707(02)00042-X.

Zwally, H. J., Schutz, R., Bentley, C., Bufton, J., Herring, T., Minster, J.-B., Spinhirne, J., & Thomas, R. (2014). GLAS/ICESat L1B Global Elevation Data, Version 34 [in Franz Josef Land]. doi:10.5067/ICESAT/GLAS/DATA126.